



HAL
open science

Multiobjective statistical learning optimization for large-scale RGB metalens

Mahmoud M R Elsayy, Mickaël Binois, Régis Duvigneau, Samira Khadir, Anthony Gourdin, Patrice Genevet, Stéphane Lanteri

► **To cite this version:**

Mahmoud M R Elsayy, Mickaël Binois, Régis Duvigneau, Samira Khadir, Anthony Gourdin, et al.. Multiobjective statistical learning optimization for large-scale RGB metalens. 2021. hal-03212349v1

HAL Id: hal-03212349

<https://hal.science/hal-03212349v1>

Preprint submitted on 29 Apr 2021 (v1), last revised 25 May 2021 (v2)

HAL is a multi-disciplinary open access archive for the deposit and dissemination of scientific research documents, whether they are published or not. The documents may come from teaching and research institutions in France or abroad, or from public or private research centers.

L'archive ouverte pluridisciplinaire **HAL**, est destinée au dépôt et à la diffusion de documents scientifiques de niveau recherche, publiés ou non, émanant des établissements d'enseignement et de recherche français ou étrangers, des laboratoires publics ou privés.

Multiobjective statistical learning optimization for large-scale RGB metalens

Mahmoud M. R. Elsayy,[†] Mickaël Binois,[†] Régis Duvigneau,[†] Samira Khadir,[‡]

Anthony Gourdin,[‡] Patrice Genevet,^{*,‡} and Stéphane Lanteri^{*,†}

[†]*Université Côte d’Azur, Inria, CNRS, LJAD, 06902 Sophia Antipolis Cedex, France*

[‡]*CNRS, CRHEA, Université Côte d’Azur, Sophia Antipolis, Valbonne, France*

E-mail: patrice.genevet@crhea.fr; stephane.lanteri@inria.fr

Abstract

Designing highly efficient multiwavelength metalens has witnessed rapid growth in the past few years owing to their fascinating and peculiar applications. The conventional modelling technique relies on optimizing the individual nanoresonators in a periodic array and synthesizing the required phase profile. Generally speaking, the traditional procedure neglects the near-field coupling between the resonators and leads to a dramatic reduction of the efficiency, particularly at the visible regime, and notably for high numerical aperture lenses. Another alternative way is to combine a numerical optimization technique with full-wave simulations to mitigate this problem and optimize the full lens. Nonetheless, this process has been frequently applied to gradient-based techniques with/without freeform shapes which generally converge to a local solution. In this work, we present for the first time a global multiobjective optimization technique based on statistical learning to optimize RGB spherical metalenses at the visible regime. The optimization procedure is coupled to our high-order full-wave solver to capture the strong near field coupling between the resonators. The first

RGB optimized lens has $8\mu\text{m}$ diameter and $NA=0.47$ and yields an average focusing efficiency of 55%. The second optimized lens has $10\mu\text{m}$ diameter and $NA=0.56$ with 45% average efficiency. Furthermore, we obtained an average focusing error as small as 6% for the RGB colors. The optimized lenses have been fabricated and characterized experimentally, where a good agreement is attained between the numerical and the experimental results. The measured average focusing efficiency are approximately, 45% and 33%, for the first and the second design, respectively. To the best of our knowledge, this is the highest focusing efficiency obtained so far for such spherical metalens with classical cylindrical pillars with $NA > 0.5$ at the visible regime.

Introduction

Metasurfaces are attracting widespread interest due to the notable distinctiveness in controlling all the light attributes in very short propagation distances compared to the standard bulky optical components.¹⁻⁵ The fundamental design principle of metasurfaces is the arrangement of subwavelength resonators with different geometrical parameters which allow for a precise control of the incoming wavefront.³⁻⁸ The novel development technology along with the versatility of metasurfaces have led to exceptional and peculiar applications⁹ in relation to sub-diffraction optical microscopy,¹⁰ nonlinear optics,¹¹ and quantum optics,¹² to cite a few examples.

During the last few years, it has been demonstrated that the precise engineering of sub-wavelength patterning is compulsory in enhancing the performance of metasurfaces in particular for highly demanding applications. Consequently, several innovative inverse design methodologies have been recently exploited to further extend the metasurface capabilities, especially for devices serving for a single performance goal.¹³⁻¹⁶ Notwithstanding, the next decade is likely to witness a noteworthy growth in the field of multifunctional metasurfaces owing to the increasing demand in designing flat optics devices with a wide variety of functionalities. This makes the exploitation of rigorous inverse design strategies which are

capable of optimizing metasurfaces with multiple functionalities a mandatory step for the next metasurface generation.

Yet, this is not a straightforward task since optimizing multifunctional metasurfaces necessitates resolving an optimization problem with multiple competing objectives and most likely includes a large parameter space. Generally speaking, two major approaches have been put forward to undertake this problem.

The first strategy is essentially based on transforming the multiobjective optimization problem into a single objective one. This is realized by merging different objectives via a classical weighted sum technique, through assigning a dedicated coefficient to each target so that the targets with higher priorities are assigned to higher coefficient values compared to the less notable objectives.¹⁷ The resulting single objective problem is then resolved by employing a standard single optimization method to converge to an optimized design based on the predefined weighted coefficients.^{18,19} Latterly, the weighted sum approach has been used to optimize various multifunctional metasurfaces devices. In most cases, the emerging single objective problem has been tackled by utilising classical evolutionary single objective techniques.²⁰⁻²³ Yet the straightforward attainable implementation of the weighted sum procedure is often impractical, especially for problems that contain several competing objectives. This approach aims at satisfying the objectives based on predefined weighted coefficients, which may not necessarily be the most suited trade-off between them.

The second methodology relies on resolving directly the multiobjective problem by adopting a dedicated numerical optimization method rather than reducing the problem to a single objective one. This approach seeks to find the optimal solution for the given set of objectives with an adapted definition of optimality. Indeed, the concept of the optimal solution in the case of multiobjective optimization is distinct from its equivalent notion in the single objective case. The latter attempts to reach the set of parameters corresponding to the most desirable fit to the objective. Nonetheless, the former aims at obtaining the set of solutions which satisfy the best trade-offs between the specified objectives. In most cases, achieving

the best fit in one objective degrades the performance of the other objectives. Thus, the essential purpose of the multiobjective optimization is to attain the set of solutions corresponding to the most suitable compromise between the objectives. This set of solutions are usually defined as the *Pareto front*, or the set of *non-dominated* solutions in the objective space. In other words, a design x is a Pareto optimal if there is no other design that is at least as good for all objectives and strictly better for at least one.

One common approach is to rely on the development of Multiobjective Optimization Evolutionary Algorithms (MOEAs).²⁴⁻³⁰ MOEAs are able to produce the global set of optimal solutions in the form of the Pareto front thanks to their stochastic nature and their ability to converge to the global solution rather than focusing in local regions. Besides, they are intrinsically based on biological evolutionary mechanisms, like mutation, selection, and crossover. This essentially broadens the search scheme during the optimization and enriches the possibilities to converge to the global Pareto front.

There exists a wide variety of MOEAs such as Genetic Algorithms (GAs),³¹⁻³³ Covariance Matrix Adaptation Evolutionary Strategy (CMA-ES),³⁴ and Particle Swarm Optimization (PSO).³⁵⁻³⁸ MOEAs have been extensively employed to optimize multifunctional electromagnetic problems in various disciplines³⁹⁻⁴² owing to their ability to deal with large parameter space and their flexibility in considering both continuous and discrete parametrization. In the field of metasurfaces, multiobjective GAs have been used to optimize wavelength selective and absorbing metasurface designs.⁴³ Moreover, advanced MOEAs have been developed for optimizing colour pixels metasurface⁴⁴ and multi-resonant nanoridges for metasurface applications.⁴⁵ Recently, a MOEA based on BORG library²⁹ has been exploited for generating a library of optimized freeform shapes,^{46,47} to synthesize metasurfaces with multiple targets.

Despite recent developments in MOEAs, there is still considerable concern about their practical use for realistic applications. Although MOEAs are capable of converging to the global set of solutions, in addition to their interesting versatility, a major defect of MOEAs

is that they are computationally demanding and subject to high overheads iterations. This major limitation makes them impractical when combined with a costly three-dimensional electromagnetic solver.

The rapid growth of applying deep learning in the field of nanophotonics and metasurfaces^{14,16,48–54} has prompted researchers to think about resorting to deep learning to solve multiobjective electromagnetic problems. The foremost concept behind deep learning is to substitute the expensive simulations by a trained network capable of predicting the relationship between the set of parameters and the corresponding electromagnetic response. Yet, similar concerns as for MOEAs have arisen since generally the training process entails a huge amount of simulations.^{55,56} Recently, novel approaches like generative models^{56–58} have been adopted to accelerate the training process. Such an approach has lately been extended to optimize multifunctional nanophotonic devices.^{59–61} Despite this interest, there is no general agreement on the relation between the number of objectives/parameters and the required number of simulations to train the network. In particular, when multiple objectives are considered, training the network might require a considerable amount of resources. Besides, the fact that the deep network is not inherently an optimization tool, it might suffer from convergence issues, notably in the case of competing objectives.

In our former work,⁶² we presented an alternative and efficient methodology based on statistical learning for optimizing single objective metasurfaces with a moderate budget of fullwave solver calls. It is known as Efficient Global Optimization (EGO).^{63–65} This method is based on surrogate modelling, which replaces the high fidelity electromagnetic evaluation process with a simpler and cheaper model for the prediction of the new designs during the optimization process. Despite the fact that EGO converges to the global solution rather than the local one, it demands fewer iterations compared to a more classical global evolutionary strategy as we demonstrated earlier.⁶² This interesting feature makes EGO an attractive optimization method for complex electromagnetic designs.

In this work, we present for the first time to the community a multiobjective optimization

based on statistical learning. We demonstrate that this method converges rapidly to the global set of optimal solutions by using an adequate number of solver calls.

The paper is organized as follows. First, we discuss the main feature of the multiobjective EGO method, by providing a simple and clear illustration of its development. Second, we apply the multiobjective EGO in optimizing the deflection efficiency of the Red, Green, and Blue (RGB) colors in a metasurface design. Despite the sophisticated competition between the three objectives, our optimization method is able to provide a single design based on a realistic configuration with more than 75% of average deflection efficiency for the three wavelengths. These results are depicted in the Supplementary information section.

Third, we extend our analysis towards the optimization of a 3D RGB achromatic metalens with moderate numerical aperture. Our numerical optimization study yields an average focusing efficiency of 45% using cylindrical nanopillars for a 3D metalens with a numerical aperture of 0.56 and diameter $\approx 10 \mu\text{m}$. In addition, we confirm that the chromatic dispersion issue is diminished, and that the three wavelengths focus at the same position with a relative focusing error of 6%. Besides, the optimized designs have been fabricated and characterized experimentally. Remarkably, we found a qualitative agreement between the numerical and the experimental results.

Multiobjective EGO

To deal with expensive black-box problems, it is common to resort to a surrogate model of the function of interest. The surrogate model provides a quick estimation to approximate the true function, which can be used to select the best candidates to evaluate next, in a sequential manner. Among other alternatives such as, for instance, support vector machines or neural networks, Gaussian process (GP) regression, also known as kriging, provides a probabilistic model. Such a model is able to predict the value at n-evaluated locations while giving an estimate of the uncertainty about this prediction. It is crucial in optimization to

balance exploration of poorly known regions of the input space (large predictive variance) with the exploitation of promising regions (low predictive mean). For more details about Bayesian optimization, we refer to Refs.^{66,67} Besides, the readers can also refer to our previous works^{15,16} where we describe the EGO steps using simplified problems in the single objective case. Below, we provide a concrete illustration of the multiobjective EGO method.

In general, the EGO method consists in two phases. The first one is the Design Of Experiment (DOE) phase, which aims at generating an initial database of designs. In essence, each of these designs is evaluated using an electromagnetic solver where the corresponding objective value is deduced. In the second phase, using the data obtained from the DOE, a Gaussian Process (GP) model is constructed for each objective, using an internal optimization process to fit the set of GP models to the DOE. The generated GP models for each objective provide a prediction of the objective values along with the parameter space but without additional further fullwave simulations. It is worth mentioning that in our case, each GP model is fitted independently to each objective, as it is commonly used in the literature for objectives that are not strongly correlated.

Once the GP models (one for each objective) are obtained, one can determine at each point in the design space the mean and the variance of the GP models. The former gives the expected values of the objectives at the given point in the design space, while the latter provides information about the uncertainty on these objective values.

Based on the statistical information afforded by the GP models, a statistical merit function needs to be established in order to identify which design (set of parameters) should be tested in the next iteration that would provide a better approximation to the Pareto front. In our case, we consider the common criterion known as the Expected Hypervolume Improvement (EHI).⁶⁸ In Fig. 1, we illustrate the role of the EHI selection criterion in the multiobjective EGO process (see Ref.⁶⁹ for more details).

In Fig. 1, we exhibit an engraving for the principle of the multiobjective optimization based on EGO. We consider here one parameter X to optimize further, we aim at minimizing

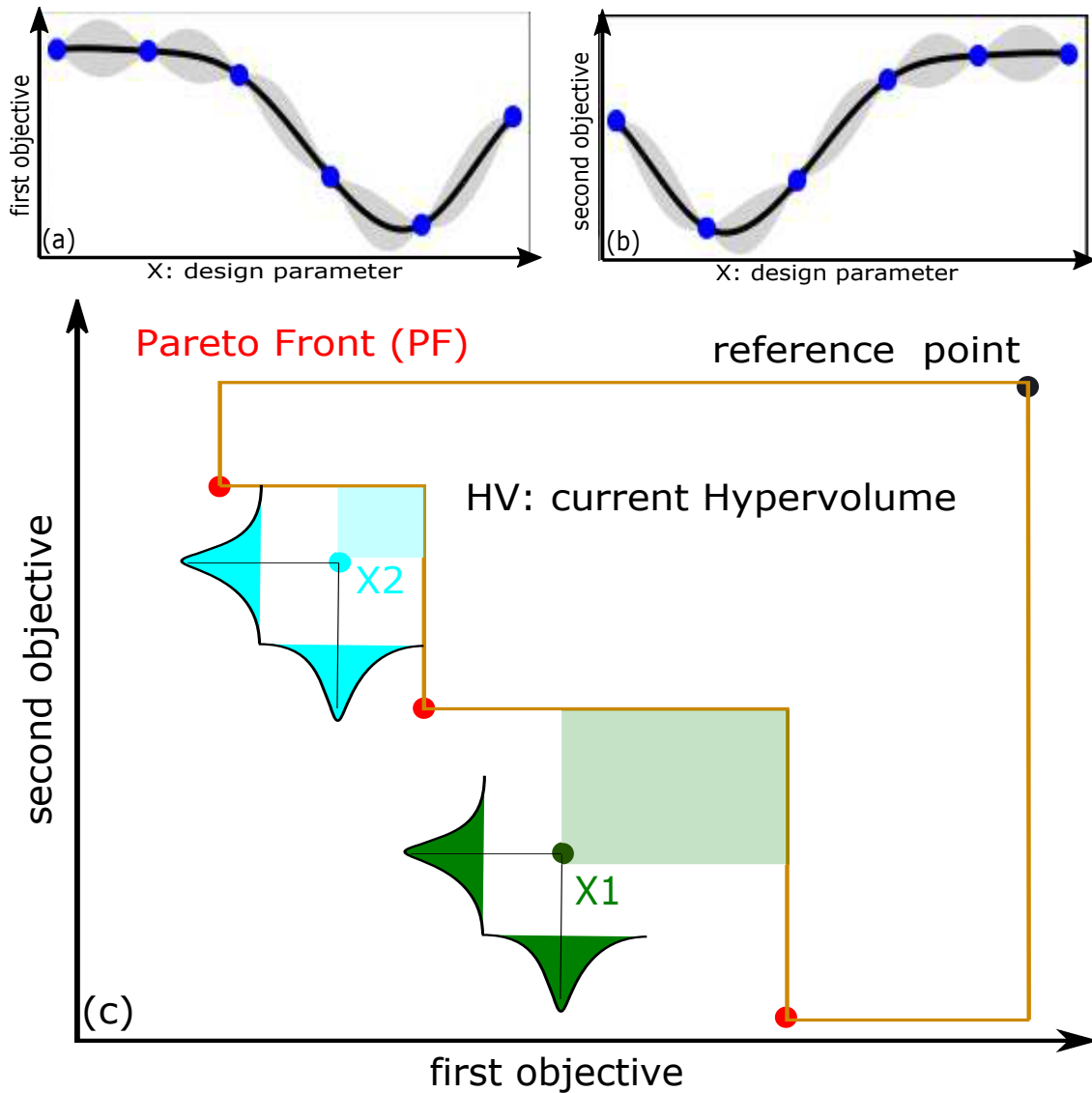


Figure 1: Illustration of the multiobjective optimization context and the expected hypervolume improvement (EHI) criterion.^{68,69} (a-b), two independent metamodels for the first and the second objective, respectively. The blue points refer to the DOEs. (c): objective space where the red points represent the existing non-dominated designs (PF). The orange region illustrates the current hypervolume (region between the current PF and a reference point). Green and cyan points refer to the predictive mean for two new designs X_1 and X_2 , respectively. Shadow regions indicate the expected hypervolume improvement from X_1 and X_2 . See text for more details.

two distinct and competing objectives. We assume 6 DOEs given by the blue points in Figs. 1(a-b). At this step, for each objective, the corresponding GP model is fitted based on the DOEs as illustrated by the black curves in Figs. 1(a-b). Furthermore, the set of non-dominated solutions (PF) are extracted and displayed in the objective space (see red points in Fig. 1(c)). Thanks to these GP models, one has information about the mean (value of the objective) and the uncertainty (variance) at each point in the design/objective space. For instance, the green and the cyan points indicate the predictive means (predictive values of the two objectives) for two novel designs X_1 and X_2 , respectively. At this step, we are interested in knowing which design will be chosen (to simulate) to converge faster to the exact Pareto front. Thus, we seek at computing the expectation of the hypervolume improvements (with a closed-form expression⁷⁰) added to the current Pareto front (red points) from each Gaussian distribution around X_1 and X_2 . One can see that the design X_1 is expected to increase the current hypervolume compared to the design X_2 as illustrated by the green and cyan shadow regions. In other words, the green point adds more improvement to the current Pareto front (red points) than the cyan one, and hence X_1 will be the next design to evaluate. We refer to Refs.,^{69,71} for more details about the EHI selection criterion.

Now, considering our application metasurface context, in the search parameter space where EHI is maximized, we extract the corresponding parameter values, and the corresponding design will be simulated using a fullwave electromagnetic solver. After that, the database is updated accounting for this new observation (construction of new GP models based on the updated database). This process is repeated until a predefined convergence criterion is reached, or when the EHI is sufficiently small. This specific statistical learning criterion makes our global optimization solver converges rapidly to the exact set of solutions. Besides, this feature demonstrates that EGO outperforms all the global evolutionary multi-objective optimizations and make it an ideal platform for time-consuming multi-functional nanoscale devices with competing objectives. In practice, we use the `GPareto`^{72,73} R package to conduct multiobjective optimization.

In the present study, we couple the multiobjective EGO with our in-house high-order fullwave electromagnetic solver based on the Discontinuous Galerkin Time-Domain (DGTD) method.⁷⁴ DGTD can be viewed as a mixture of a classical (continuous) Finite Element Time-Domain (FETD) and the Finite Volume Time-Domain (FVTD) method. We exploit a high-order DGTD-based solver that we have recently developed, and which has been specifically designed for the simulation of nanoscale light-matter interaction problems.⁷⁵ This DGTD fullwave solver is implemented in the DIOGENeS⁷⁶ software suite, which is programmed in Fortran 2008 and is adapted to high performance computing systems. It is worth mentioning that the use of this high-order DGTD solver is fully justified in this work. First, throughout this work, we rely on multi-wavelength metasurface designs, accordingly, it is more practical to work with a time-domain solver where the objective values with regard to a wavelength range is obtained with a single simulation run. Second, we have illustrated recently that our solver is crucial and efficient in assessing near field coupling between the neighbouring elements, which is a fundamental factor in designing high efficient nanophotonic based designs.^{15,77} Finally, due to the adaptability of our high-order DGTD solver in handling large-scale problems, the number of mesh cells is considerably reduced compared to other time-domain methods like the Finite-Difference Time-Domain (FDTD). These attractive features of our DGTD solver implemented in the DIOGENeS⁷⁶ software suite unitedly with the multiobjective EGO method offer an ideal platform methodology for optimizing multifunctional metasurface based designs.

As proof of concept, we employed the multiobjective EGO in an attempt to optimize a beam steering metasurface at three different wavelengths simultaneously. The results are shown in the supplementary information section. However, in what follows, we focus on presenting our numerical and experimental results for large-scale metalens design at the visible regime.

Results and discussion

3D large-scale RGB metalens

In this section, we employ our methodology to the design of a large-scale 3D achromatic metalens with high numerical aperture. In conventional optical lenses, the chromatic dispersion can be reduced by stacking various lenses together, however, the overall system becomes bulky and costly to produce. In comparison, metasurfaces offer the opportunity to alleviate the chromatic dispersion based on much thinner architectures. Yet, this is not a straightforward task due to the intrinsic dispersion nature of the constituting elements.

The conventional approach in optimizing 3D metalenses is based on synthesizing the phase. This procedure necessitates tuning the individual elements in order to engineer their transmission and their phase shift response, more precisely, for ensuring a 2π phase shift change to control the incoming wavefront. However, in order to deliver the focusing at a given fixed position F , a varying phase profile (changing in the radial direction) across the metasurface is required:

$$\phi(\omega; x, y) = -\frac{\omega}{c} \left(\sqrt{x^2 + y^2 + F^2} - F \right). \quad (1)$$

Here, ω is the angular frequency, x , y represent the position of each individual element, and c is the speed of light. Clearly, Eq. 1, is a frequency-dependent equation. In other words, in order to ensure the broadband focusing for a given fixed focal distance F , one has to devise the best combination of the elements to decrease the chromatic dispersion and ensure the broadband focusing at the same position with high performance. Several attempts have been made to derive rigorous selection criteria to alleviate the chromatic dispersion issue. The principal shortcoming of the classical synthesizing technique is the ignorance of the near field coupling, which is the main cause of degradation of the focusing efficiency. Numerous exciting 3D broadband lenses have been optimized based on this synthesizing procedure,^{78–82} among others. Yet, the overall efficiency drops dramatically for lenses with $NA > 0.5$ due

to the rapid change of the phase required.

Optimizing the full metalens is another alternative manner to enhance the performance. Nevertheless, this approach requires both a rigorous fullwave solver to account for the near field coupling and an efficient optimization algorithm. In the 3D case, few works have been published lately based on optimizing freeform shapes.⁸³⁻⁸⁵ Despite the versatility offered by the aforementioned freeform full optimization methodologies, they yield devices with sophisticated patterns which are difficult to match by the current fabrication technologies. Another attractive computational frameworks are proposed in Refs.⁸⁶⁻⁸⁸ based on gradient based architecture. Yet, gradient-based techniques most likely lead to local solutions rather than obtaining the global designs.

It is worth mentioning that the optimization of 2D metalenses (cylindrical), where focusing is mainly ensured along two directions solely, is extensively considered in the literature. In this 2D case, exciting works have been published recently^{83,84,88-92} based on different architectures for various numerical apertures. In the present work, we focus only on 3D spherical designs where the focusing is maintained along the three spatial dimensions at the visible regime.

Our work is distinct from what has been recently reported in the literature, where the metalens is either optimized via the synthesizing procedure or optimized based on freeform shapes or with gradient-based strategies. First, we consider cylindrical shapes which are easy to fabricate, and we take into account the fabrication constraints which are usually hard to satisfy for most freeform optimized lenses. Second, we optimize almost all the meta-atoms and account for the strong near field coupling (by tuning the distances between them) that could arise, unlike the classical synthesizing process. Finally, we rely on a rigorous methodology by combining a global optimization method with a high-order DGTD solver to converge to the global solution and indeed treat the large-scale problem with a moderate number of degrees of freedom.

In Tab. 1, we summarize results of recent works dealing with 3D achromatic metalens

design (including our current work). For more details about the fundamental limitations of achromatic metalenses, we refer to Refs.^{93,94}

Table 1: Comparison of 3D achromatic spherical metalens designs. Here ^(a) refers to the experimental results, while ^(b) is for the numerical simulation results.

NA	Diameter (μm)	Building blocks	Bandwidth	Average focusing efficiency
0.12	20.0	Fishnet	640-1200	61 ^(a) % ⁸¹
0.2	26.6	Anisotropic unit cell	460-700	30 ^(a) % ⁹⁵
0.25	7.5	Freeform	480,650,850	63 ^(b) % ⁸³
0.27	20.0	Hybrid elements	1000-1800	60 ^(a) % ⁸²
0.26	6.0	Cylinders	400-700	60 ^(b) % ⁹²
0.47	8.056	Cylinders	480,550,640	55 ^(b) % & 43.46 ^(a) % (this work)
0.56	10.22	Cylinders	480,550,640	45 ^(b) % & 33.46 ^(a) % (this work)

In this work, we aim at optimizing a 3D metalens with NA between 0.45 and 0.6 to focus the RGB colors at the same focal plane with the maximum feasible efficiency as depicted in Fig. 2(a)). In other words, we seek to achieve the most suitable compromise between the chromatic dispersion and the efficiency for a given fixed focal distance.

Our 3D metalens is composed of concentric rings of cylindrical nanopillars of GaN as depicted in Fig. 2(b). The height of the cylinders is fixed as 1000 nm. As a first design, we consider 12 concentric rings (apart from the central cylinder), in which the number of the cylinders in each ring (fixed during the optimization) increases when moving towards the outer rings. In general, we have roughly 407 cylinders in the whole metalens. The distribution of cylinders in each ring is summarized in Tab. 3 in the supplementary information.

Nevertheless, in order to reduce both the computational cost and the number of optimization parameters, we rely on the symmetry properties of the 3D lens and consider only one-quarter of the structure as shown in Fig. 2(c) (a 3D view is presented in Fig. 10(a) in the supplementary information together with some details about the symmetry properties). Additionally, we assume that the cylinders in each individual ring share the same diameter. Consequently, we consider only optimizing one row of cylinders along the radial direction together with the distances between the rings, as indicated in Fig. 2(c) by the yellow cylinders and the black arrows, respectively. Furthermore, in our design, we fix the diameters

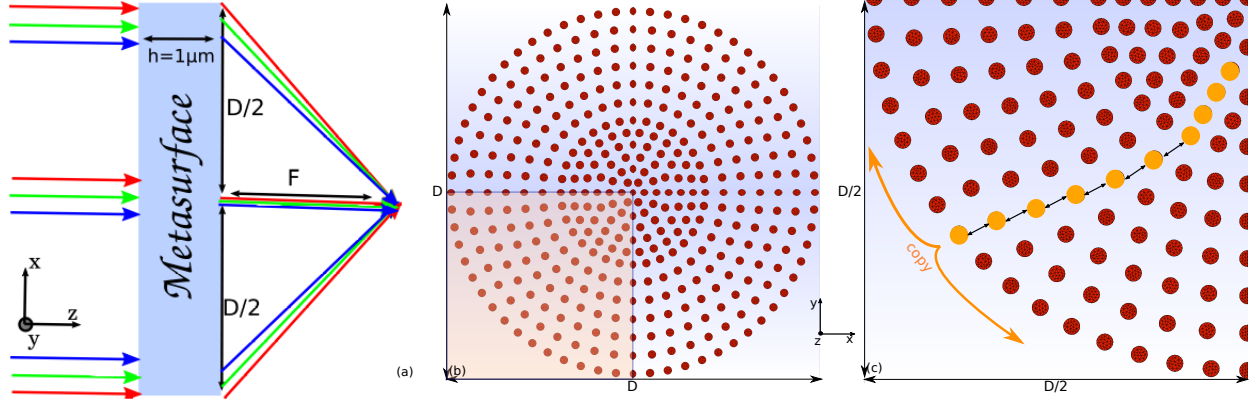


Figure 2: (a): schematic view of the 3D achromatic metalens in the $x - z$ plane. The metalens aims at focusing the three colors at the same focal distance F . The diameter of the metasurface is D and the thickness is fixed as $h = 1000$ nm. (b-c): $x - y$ plane for the 3D metalens under investigation, (b) for the whole metalens, and (c) for one-quarter of the geometry (shadow region in (b)). The metalens consists of concentric rings of cylindrical GaN nanopillars (red region) placed on top of semi-infinite Al_2O_3 of dimension $10 \mu\text{m} \times 10 \mu\text{m}$, which is fixed during the optimization. The number of cylinders in each ring is given in the first two columns in Tab. 3. The 16 optimization parameters are depicted in (c), 10 diameters represented by the yellow cylinders and 6 parameters for the distances between the outer rings (black arrows).

of the cylinders in the first three rings together with the distances between the first seven rings. This is an admissible assumption since the central rings are expected to delay the light in the centre of the lens. Hence, one can arrange the distances between them to the minimum limit (in our case 100 nm is the minimum feature size for the distance between rings). Moreover, the centre cylinder has a fixed diameter of 220 nm, and the cylinders in the three sequential rings are assumed to have fixed diameters as 200 nm. In summary, in this configuration (Fig. 2(c)), we optimize only 16 parameters: 10 diameters represented by the yellow cylinders (vary between 90 nm and 200 nm) and 6 distances between the outer rings indicated by the black arrows (vary between 100 nm and 250 nm).

It is worth mentioning that the near field coupling between all cylinders is taken into account during each optimization iteration to compute the objective functions rigorously. Besides, one notice that the diameter of the lens is varying based on the position of the last ring. Nevertheless, the focal distance F is fixed during all the iterations as $7.5 \mu\text{m}$. For this

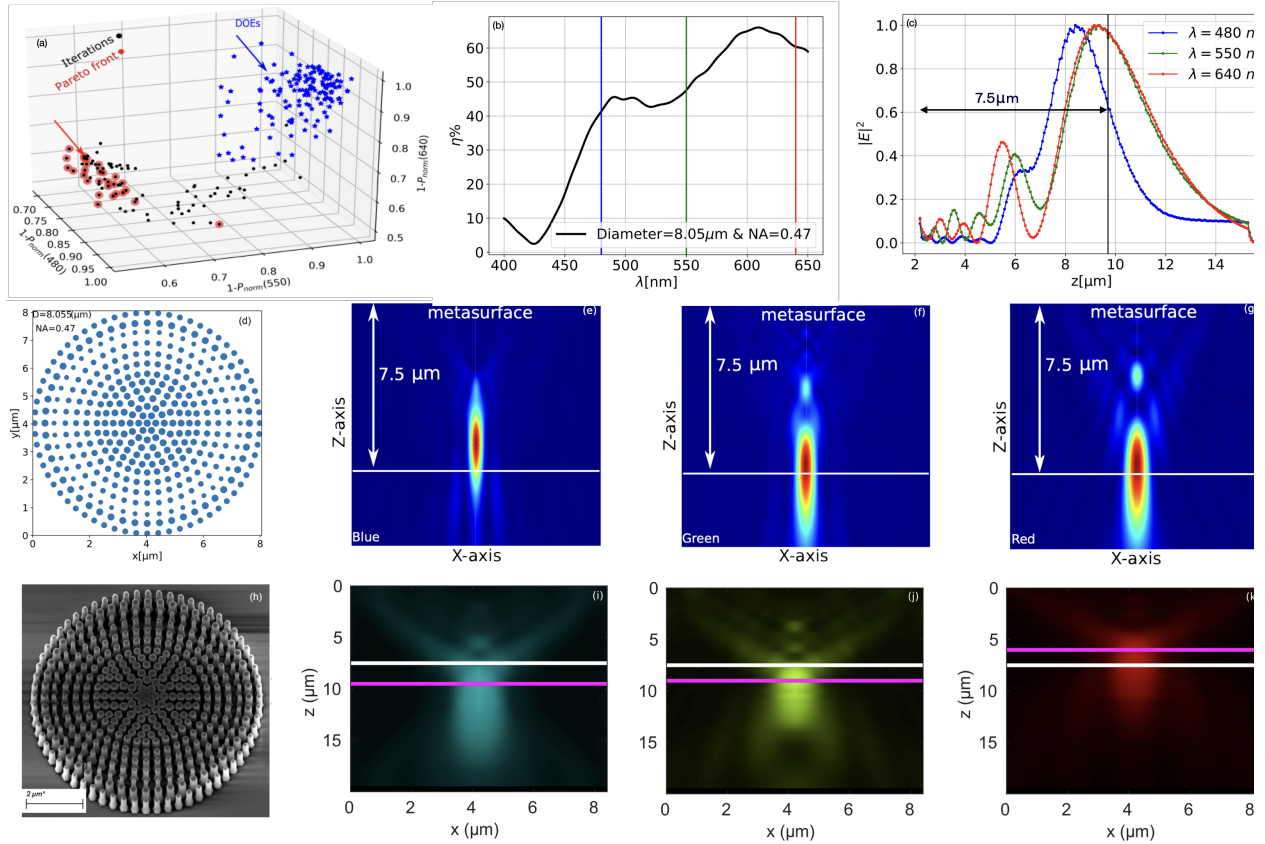


Figure 3: (a): optimization results for the first metalens design with 16 optimization parameters, composed of 12 concentric rings as shown in Fig. 3(d). The blue points refer to the 90 designs in the DOE database, the black ones indicate the optimization iterations. The red points represent the Pareto front (see the text for more details). We chose one of the best designs along the Pareto front (red arrow in (a)), where the three objectives are maximized simultaneously. The diameter of the chosen lens is $8 \mu\text{m}$ (the associated parameters are given in Tab 3). (b): numerical focusing efficiency of the optimized chosen lens. The efficiency is calculated as the ratio of the power at the focal plane to the power passing through an aperture of diameter $8.055 \mu\text{m}$ (diameter of the optimized lens). The three vertical lines refer to the three wavelengths considered during the optimization. The numerical convergence is studied in Fig. 10(b). (c): cut along z at the center of the lens for the RGB colors. The vertical line refer to the target focusing position F . (d): indicate the x - y profile of the optimized design. (e-g): numerical intensity profiles at the x - z plane. (h): SEM of the fabricated lens and (i-k) illustrate the experimental focusing intensity at the x - z . The intensity is measured at $\lambda = 490 \text{ nm}$, $\lambda = 550 \text{ nm}$, and $\lambda = 660 \text{ nm}$ for the blue, green, and red colors, respectively.

first design, we aim at maximizing the power at the focal plane ($z = 7.5 \mu\text{m}$) for the blue color at $\lambda = 480 \text{ nm}$, green color at $\lambda = 550 \text{ nm}$, and for the red color at $\lambda = 640 \text{ nm}$. Without loss of generality and for normalization purpose, we rescale the power at the focal plane to the power passing through a circular aperture of diameter $10 \mu\text{m}$ (fixed during the optimization process). Once the power at the focal plane is optimized for the three wavelengths, we pick up the correct diameter (for the optimized design) and we calculate the exact focusing efficiency. In our case, the focusing efficiency is estimated as the ratio between the power in the focal plane (circle or radius 800 nm) divided by the power passing through a circular aperture with diameter D . The diameter is defined after determining the optimized parameters. Then, the actual numerical aperture is computed. It is worth mentioning that the diameter of the focal plane is fixed for the three wavelengths and is considered as three times the average of the theoretical full width at half maximum (FWHM) of the three wavelengths. Indeed, this might introduce small bias for the focal distance, however, as we shall see below, the overall bias is minimal. Based on the above procedure and the given fixed focal distance $F = 7.5 \mu\text{m}$, the NA is varying roughly between 0.32 and 0.6. As we shall show next, one might improve the results by adding supplementary rings that ultimately increase the NA and afford more control over the dispersion, this reducing the chromatic dispersion.

In Fig. 3(a), we present the optimization results for the first lens with 12 concentric rings. The normalized power is denoted as P_{norm} . We are considering a minimization problem, thus the main objective here is to minimize $1 - P_{norm}$ for $\lambda = 480 \text{ nm}$, $\lambda = 550 \text{ nm}$, and $\lambda = 640 \text{ nm}$. In this particular example, we optimize 16 parameters for satisfying 3 objectives, thus, we consider a DOE database with 90 elements (blue points) for the initial learning process. These points are then used to construct 3 metamodels (one for each objective). Once the metamodels are built, the EHI criterion (see our discussion above about the EHI selection criterion) is used to select the next design to be simulated. The optimization iterations are outlined by the black points in Fig. 3(a) while the Pareto front is given by the red points. In the present case, 180 iterations are enough to capture the Pareto front (the convergence

results are depicted in Fig. 11 in the supplementary information section). We pick one of the best middle points along the Pareto front where the minimization of the three objectives is ensured. The corresponding lens is shown in Fig. 3(d). We have found that the optimized design yields a metalens with diameter $D = 8.055 \mu\text{m}$, which gives a numerical aperture of $NA = 0.473138$. Accordingly, based on this diameter, we computed the power passing through a circular aperture with this $D = 8.055 \mu\text{m}$ as a reference power to estimate the actual focusing efficiency of the metalens. The focusing efficiency of the metalens is plotted in Fig. 3(b) where the associated values are 42%, 49%, and 60% for the blue, green, and red colors, respectively.

Fig. 3(c) refers to the cut along z direction. Furthermore, the estimated relative focusing error along z is envisaged. For this first design, the numerical results reveal that a 4% error is obtained for the green and red colors, however, for the blue one, the relative error is approximately 13%. This can be inferred from the focusing intensity at the $x - z$ plane depicted in Figs. 3(e-g). Another alternative approach will be presented below to improve the performance.

Besides, based on our fabrication facilities, we managed to fabricate the optimized lens as shown on the SEM image in Fig. 3(h). We remind the reader that the optimization provides a lens of diameter $D = 8.055 \mu\text{m}$, further the maximum aspect ratio is approximately of 10 (ratio between the smallest diameter and the height of the cylinders). Indeed, these constraints yield a challenging fabrication environment. The fabrication process is given in the supplementary information section. The fabricated lens has been characterized using the experimental setup given in Fig. 12 (see Ref.⁹⁶ for more details). The x-z experimental intensity maps are depicted in Figs. 3(i-k), where the average relative focusing error is estimated as 19% (horizontal white line for the predefined focal length, while the purple line refers to the actual focal length). The tendency of the focal lengths are in good agreement with the numerical results, except for the blue light where the tendency is inverted, i.e., the calculated focal length is shorter than the expected one (Figs. 3(e)) while it is longer

for the measurements (Figs. 3(i)). This can be explained by the fact that the fabrication imperfections, i.e., deviations from the design diameter of the pillars, have more impact on the device characteristics for shorter wavelengths. To quantitatively compare the numerical and experimental results, we estimated the experimental focusing efficiencies of the lens at the three wavelengths (44,67% for the blue, 38.65% for the green and 47,35% for the red colors, respectively). where the average focusing efficiency is estimated as 43.55%. The experimental focusing efficiencies have been estimated as the ratio between the power at the focal plane within an aperture of a diameter defined by the FWHM of the experimental focusing spot and the in-pinging power within an aperture defined by the diameter of the lens (see more details in Supplementary Information). The measured and numerical focusing efficiencies have the same tendency as a function of the wavelength. However, the measured efficiencies are slightly lower than the numerical ones. This can be attributed to the fabrication imperfections and the losses due to the high diffraction effects from the micro-sized lens.

It is worth noting that the experimental focal spots are broader than the numerical spots (see Fig. 13 in the supplementary information section). This is due to the fact that the experimental and numerical focal spots are determined differently. The numerical focal spot corresponds to the diffraction limited spot or equivalently point spread function (PSF) of the lens. It is determined by considering a plane wave (point source at the infinity) as an incident light beam. However, the experimental focusing spot corresponds to the image of the considered source in our experiments. Its size is determined by the extent of the diaphragm D2 of the illumination system as depicted in Fig. 12 in the supplementary information section. In the following, we present an alternative way to enhance the performance of this design and further diminish the chromatic dispersion and increase the numerical aperture.

In order to further promote the focusing performance of the optimized lens shown in Fig. 3(d), we propose a supplementary step as illustrated in Fig. 4(a). In this figure, we keep the first 11 rings obtained from the previous design and append three additional rings to the

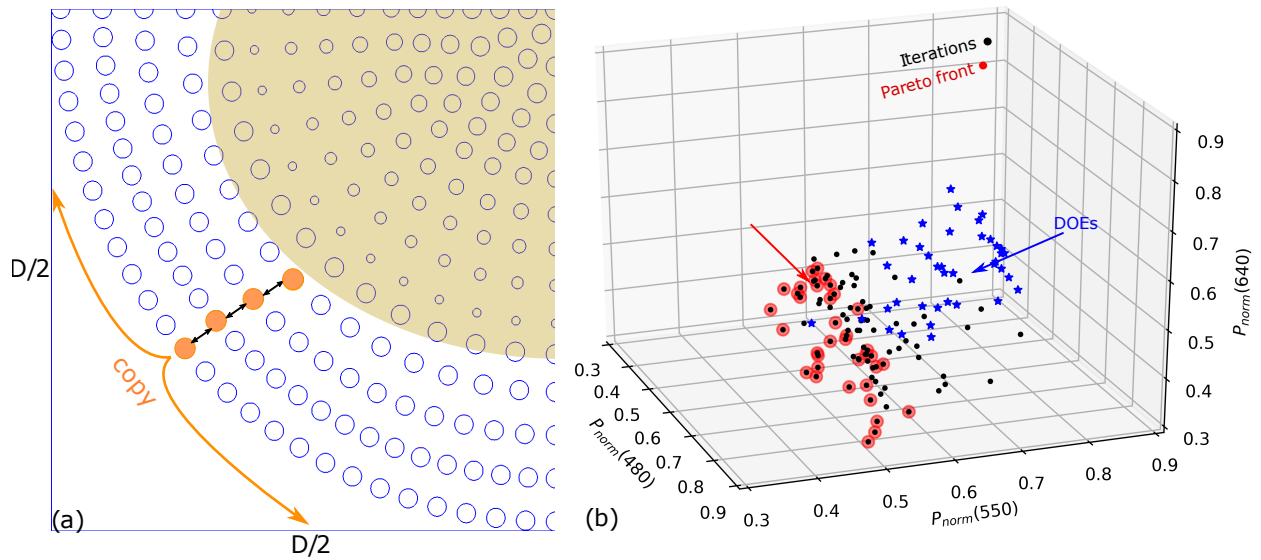


Figure 4: Extended metalens with a larger diameter and a reduced set of parameters. (a): sketch of the extended diameter lens, where the central part is fixed from previous optimized design given in Fig. 3(d) as it is represented by the shadow region. We relax the diameter of the last ring in Fig. 3(d), and add 3 more rings. In total we optimize only 7 parameters; 5 diameters (orange cylinders) and three other parameters for the distances between the outer rings (black arrows). (b): illustrates the optimization results in the second case. Here we considered 50 DOEs (blue points) and 150 iterations (black points). The Pareto front is illustrated by the red points, i.e., the set of non-dominated designs. The red arrow, refers to the results presented in Fig. 5.

outer part of the lens. The outermost ring in Fig. 3(d) is relaxed and will be combined with the additional three rings as shown in Fig. 4(a). The shadow region indicates the optimized part of the former design. While the diameters of the four highlighted cylinders indicate the optimization parameters together with the distances between the additional rings symbolized by the black arrows. Similar to the previous design, all the cylinders in the same ring are sharing the same diameter. Furthermore, the focal distance is fixed at $7.5 \mu\text{m}$ as with the previous design.

The proposed extra rings enlarge the diameter of the lens, hence renders more dispersion control for the three wavelengths. Accordingly, the numerical aperture increases. Besides, the computational cost is reduced since only 7 parameters are considered instead of 25 (for the full lens with the extra rings). The optimization results are given in Fig. 4(b), where the DOE, optimization iterations, and Pareto front are given in blue, black, and red colors, respectively.

At this stage, we are interested in obtaining a design where the three objectives are maximized. Therefore, we chose one of the best middle points along the Pareto front. The corresponding design yields a lens of diameter $D = 10.22\mu\text{m}$. This diameter is slightly larger than the one obtained from the previous design. Moreover, the numerical aperture becomes 0.56 instead of 0.47 for the previous device (the fabricated lens is exhibited in Fig. 5(c)). Based on this diameter $d = 10.22 \mu\text{m}$, we numerically estimated the focusing efficiency of the lens. As illustrated in Fig. 5(a), the computed focusing efficiencies are almost 43%, 41%, and 47% for the blue, green, and red colors, respectively. To the best of our knowledge, this is the highest focusing efficiency obtained for RGB colors for a 3D metalens with $\text{NA}=0.56$ (see Tab. 1). Besides, we rely on classical nanopillars that are easy to fabricate instead of the complex freeform geometries that might bring high efficiency while being more difficult to fabricate.

Moreover, the cut along z -axis provided in Fig. 5(b) unitedly with the numerical intensity profiles represented in Figs. 5(d-f) reveal that the chromatic dispersion effect is diminished

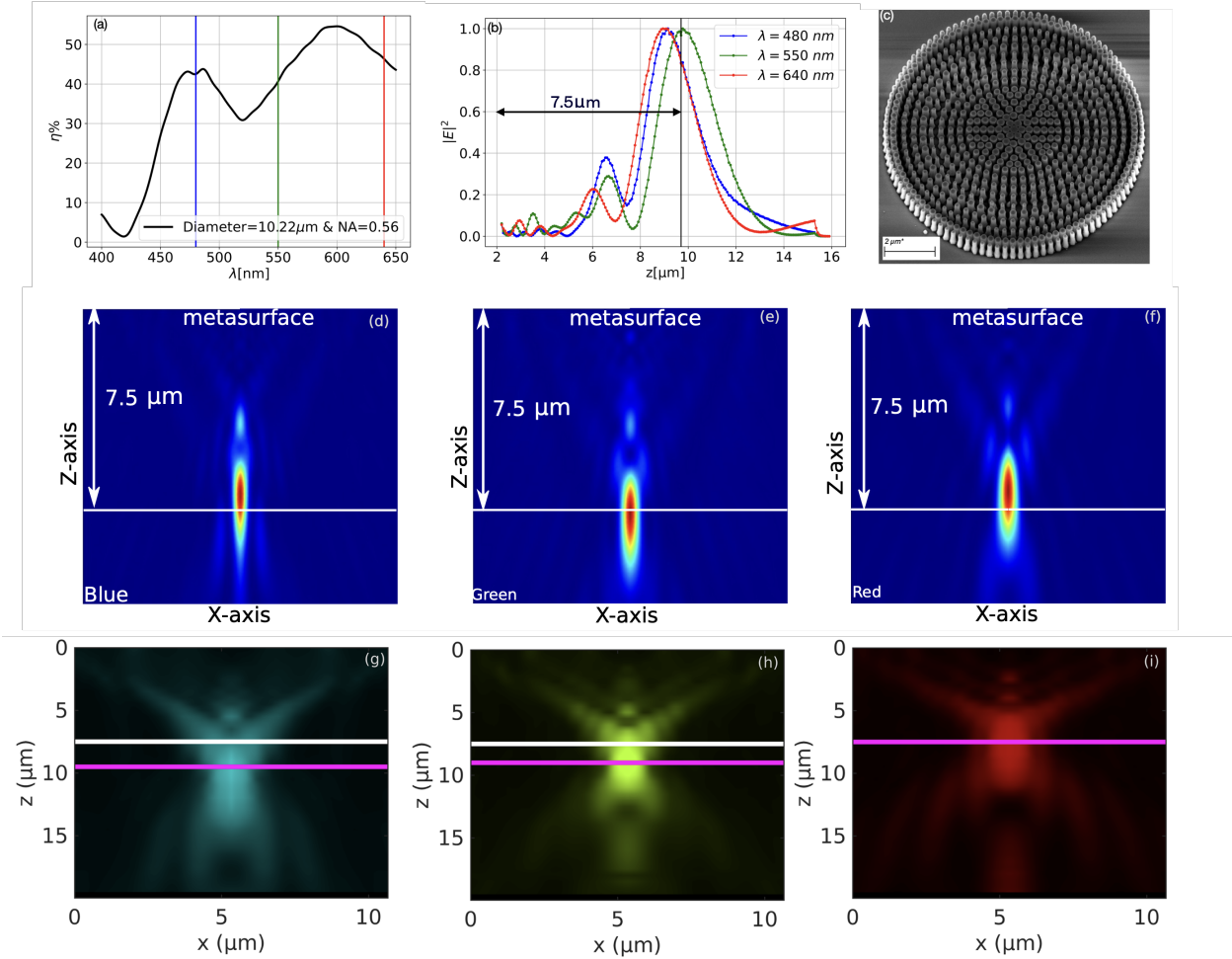


Figure 5: Optimization results for the extended design with 7 optimization parameters, composed of 15 concentric rings shown in Fig. 4(a). The results corresponds to one of the best design along the Pareto front (red arrow in Fig. 4(b)), where the three objectives are maximized simultaneously. The diameter of this lens is $10.22 \mu\text{m}$. Moreover, the full set of parameters are given in Tab. 4 in the supplementary information section. (a): provides the focusing efficiency of the optimized lens. The efficiency is calculated as the ratio of the power at the focal plane to the the power passing through an aperture of diameter $10.22 \mu\text{m}$. The three vertical lines refer to the three wavelengths considered during the optimization. (b): cut along z at the center of the lens for the RGB colors. The vertical line refers to the target focusing position along z ($z = 7.5 \mu\text{m}$). The fabricated lens is depicted in (c), besides, the corresponding intensity profiles at the $x - z$ plane is given in (g-i), where the intensity is measured at $\lambda = 490 \text{ nm}$, $\lambda = 550 \text{ nm}$, and $\lambda = 660 \text{ nm}$ for the blue, green, and red colors, respectively. The numerical focusing intensity for each color are drawn in (d-f).

compared to the previous lens. In other words, the numerical relative error for the focusing at a specific position $z = 7.5 \mu\text{m}$ is decreased for the three wavelengths. More precisely, the relative focusing error for the blue, red colors is 6.1%, while for the green one is 0.5%. This relative error of 6.1% could be due to the bias introduced from the definition of the output plane, as we argued above. Interestingly, our experimental results depicted in Figs. 5(g-i) confirms the decrease of the chromatic dispersion compared to the previous results presented in Fig. 3 (i-k). The average measured focusing efficiency is approximately 33%. The discrepancy between the measured focusing efficiency and the numerical one could be due to the fabrication imperfections associated with the challenging fabrication of the $10\mu\text{m}$ diameter lens. Generally speaking, the diminishing of the chromatic dispersion, together with the average focusing efficiency achieved, illustrate the potential of our design based on simple cylindrical building blocks to maintain high focusing efficiency (relative to the numerical aperture) and also alleviate the chromatic dispersion issue for the RGB colors.

In Fig. 6, we further demonstrate the versatility of our numerical methodology mutually with our fabrication abilities. We imitate another design along the PF shown in Fig. 4 (b). In this special case, we focus solely on optimizing the red color. As it can be seen in Fig. 6 (a), the focusing efficiency is roughly 67%, while it is dramatically reduced for the other colours. The enhanced focusing efficiency can be understood from the cut along z-axis drawn in Fig. 6 (b), where only the red colour is focused at the desired focal plane (see also the field maps in Figs. 6 (d-f)). Thanks to our fabrication platform, the fabricated design presented in Fig. 6 (c), only focuses the red color at the desired focal plane as evidenced in Figs. 6 (g-i) and the measured focusing efficiency for the red color is $\approx 45\%$ ($\approx 26\%$ for the blue and $\approx 22\%$ for the green as expected from the numerical results). The above results represent another proof to validate both the numerical and the experimental results obtained.

Indeed, reducing the numerical aperture could increase the focusing efficiency of the lens as demonstrated in earlier works⁸¹ with a numerical aperture below 0.2. However, for a 3D lens based on cylindrical nanopillars, it is challenging to compensate the chromatic dispersion

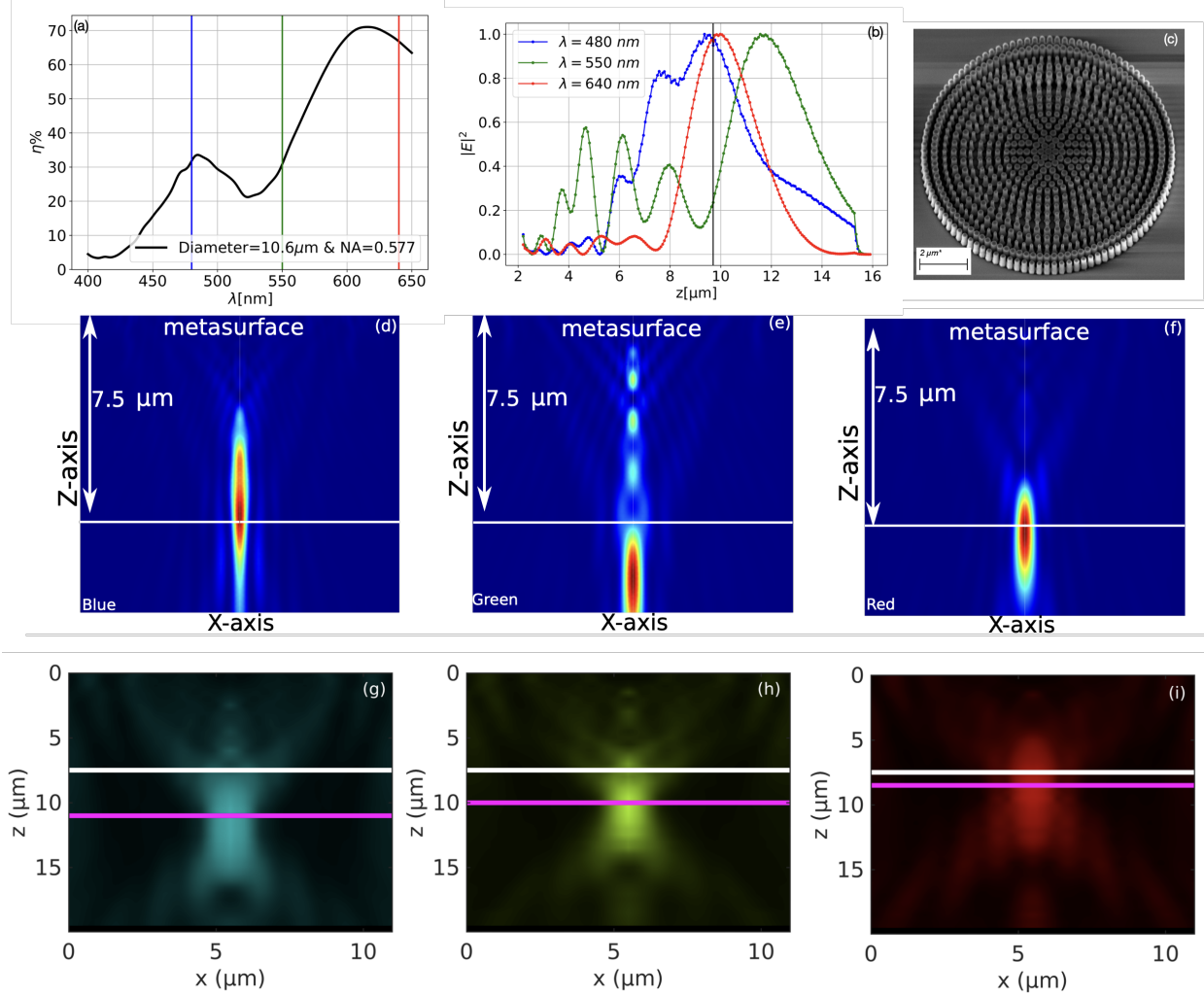


Figure 6: Optimized design for focusing the red color. The diameter of this lens is $10.66 \mu\text{m}$ as indicated in. Besides, the full set of parameters are given in Tab. 5. (a): provides the focusing efficiency of the optimized lens, where it is maximized for $\lambda = 640$ (approximately 69%). (b): cut along z at the center of the lens for the RGB colors. The vertical line refers to the target focusing position along z ($z = 7.5 \mu\text{m}$), where the red color achieves its maximum (c): represents the fabricated lens. (d-f): numerical intensity profiles along $x - z$ plane for the three optimized wavelengths. (g-i): refer to the experimental intensity profiles for the three colors.

and maintain high power efficiency for a numerical aperture above 0.5. In our future work, we will extend this work to further increase the numerical aperture by changing either the material/shape of the building blocks, or even introduce new degrees of freedom to further control the dispersion.

Conclusion

In this work, we present to the metasurface community a global statistical multiobjective optimization. In addition to its global feature, this method converges rapidly to the global set of optimal solutions using an adequate number of iterations, unlike the traditional multiobjective optimization techniques. The potential of this technique has been demonstrated by optimizing the RGB beam steering metasurface at the visible regime. Despite the inherent competing nature of the objectives, our optimization method can provide a single design based on a realistic configuration with more than 75% of average deflection efficiency with only 150 iterations (see supplementary information section). These unique features make our optimization method an ideal candidate for optimizing various multifunctional metasurface configurations.

We further considered an exciting multiwavelength spherical metalens configuration at the visible regime. The main objective was to focus the RGB colors at the same focal plane and maximize the focusing efficiency for the three colors. In this study, we aim at optimizing spherical metalens with $NA > 0.5$ using classical cylindrical nanopillars with the highest possible focusing efficiency.

Unlike the conventional modelling technique, we optimized nearly all the nanoresonators and considered the strong near field coupling between them. We optimized different lenses with different numerical apertures. the first design consists of 13 concentric rings that provide a lens with diameter $\approx 8 \mu\text{m}$ and a numerical aperture of 0.47 with 55% average focusing efficiency and 13% focal error. We further increased the performance by adding

4 supplementary rings. In this particular case, our numerical optimization study yields an average focusing efficiency of 45% using cylindrical nanopillars with a numerical aperture of 0.56 and diameter $\approx 10 \mu\text{m}$. Furthermore, we confirm that the chromatic dispersion issue is diminished and that the three wavelengths focus at the same position with a relative focusing error of 6%. We have also benefited from the capabilities of our multiobjective, such that without additional optimization, one can extract from the Pareto front the designs which focus only on one of the objectives. In our case, we extracted the best design to focus only on the red color which yields and focusing efficiency of 60

Furthermore, despite the challenges associated with the fabrication of the micro-diameter lenses and the high aspect ratio required, we managed to fabricate and characterize experimentally the three optimized lenses mentioned above. Interestingly, we found a good agreement between the numerical and the experimental results. First for the RGB designs, we obtained an average measured focusing efficiency of 43.46% ($NA = 0.47$) and 33.6% ($NA = 0.56$). Besides, we fabricated the design that focuses only on the red color, interestingly, the fabricated lens focuses as well the red color only with 45% ($NA = 0.57$) focusing efficiency. The above results validated both the numerical and the experimental findings. To the best of our knowledge, this is the highest focusing efficiency obtained in such spherical metalens configuration with $NA > 0.5$.

Acknowledgement

The authors acknowledge support from French defence procurement agency under the ANR ASTRID Maturation program, grant agreement number ANR-18-ASMA-0006-01. Numerical experiments presented in this work have been conducted on two HPC (High Performance Computing) resources: on one hand, the Occigen supercomputer of CINES under the resource allocation 2020-A0080610263 made by GENCI and, on the other hand, the PlaFRIM experimental testbed, supported by Inria, CNRS (LABRI and IMB), Université de Bordeaux,

Supporting Information Available

Optimizing of RGB light deflector

As a state of the art illustration, we employ the multiobjective EGO in an attempt to optimize a beam steering metasurface at three different wavelengths simultaneously. We aim at designing a highly efficient Red, Green, and Blue (RGB) light deflector based on a realistic configuration. In order to realize this task, we design a metasurface composed of rectangular Gallium Nitride (GaN) on top of a semi-infinite Al_2O_3 substrate (see red and green regions in Fig. 7(a), respectively). We consider five rectangular nanopillars in a supercell, with a period corresponding to 1500 nm along y direction, while along x direction, we chose a period of 190 nm to limit the diffraction in the substrate, especially for short wavelengths. The height of the rectangular pillars is fixed as $h = 1000$ nm. In this study, a normal incident plane-wave with electric field polarized along y axis is injected from the substrate. The width of each rectangular nanopillar along x is kept fixed during the optimization together with the distance between any two neighboring ridges as 100 nm and 90 nm, respectively. In order to control the phase dispersion in the $y - z$ plane, we vary the thicknesses of the rectangular nanopillars along y (represented by the white arrows in Fig. 7(a)). It is worth mentioning that the minimum width change is considered as 90 nm, which corresponds to minimum feature size for the GaN fabrication with height= 1000 nm.

The main objective is to maximize the light deflection efficiency for the first order mode (in the y - z plane) for the RGB colors. We define three different intervals for each color. For the blue color, we aim at optimizing the average efficiency (η_{avg}) in the wavelength range (450 – 480) nm. For the green color, we consider the wavelength window (520 – 550) nm, and finally for the red color, we pick the wavelength interval (620 – 650) nm. In other words, in

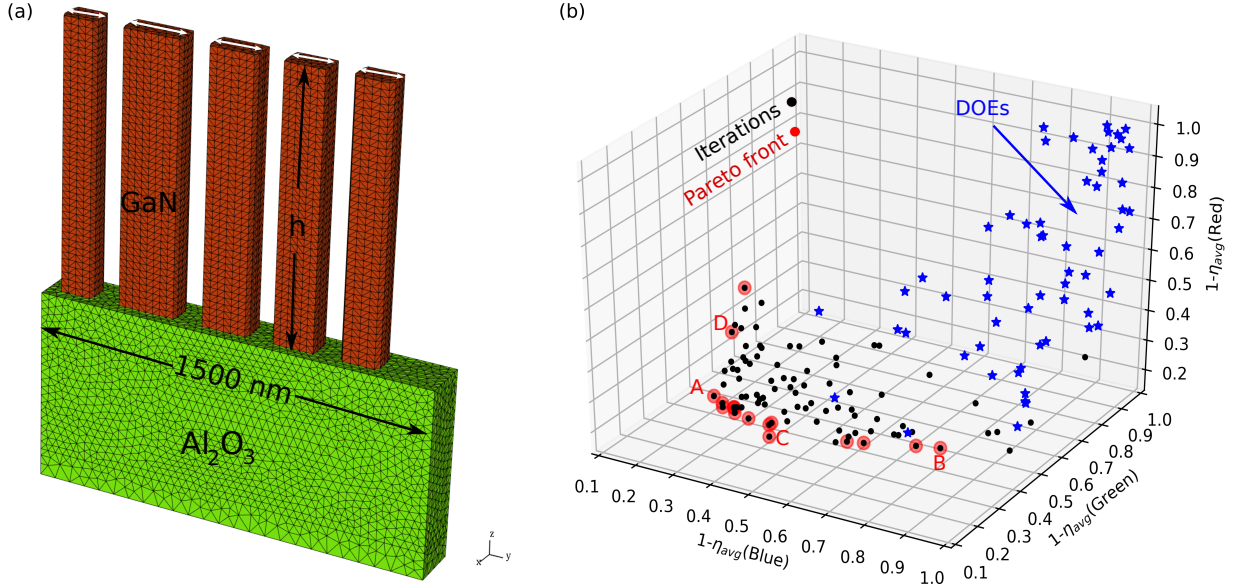


Figure 7: Optimization results for the RGB light deflector. (a): geometry under consideration, composed of five rectangular nanopillars (red regions) of GaN placed on top of a semi-infinite substrate made of Al_2O_3 (green region). The height of the pillars is fixed as $h = 1000$ nm, their widths along x are also fixed as 100 nm. The period of the super-cell along y is 1500 nm, while along x is associated to 190 nm. The optimization parameters are represented by the white arrows (widths of the pillars along y direction). (b) indicates the optimization results, where the blue points refer to the 60 DOEs. The black points are for the optimization iterations (90 points), while the red circles indicate the Pareto front. A-D letters refer to 4 designs along the Pareto front that will be considered in Fig. 8.

our optimization framework (minimization problem), we consider five parameters (width of each pillar along y) and three objectives ($1 - \eta_{avg}(\text{Blue})$, $1 - \eta_{avg}(\text{Green})$, and $1 - \eta_{avg}(\text{Red})$).

As we have explained above, the primary step in the EGO framework is to construct the design of experiments (DOEs) database. In this particular example, we have considered 60 elements in the DOE database (the corresponding objective function values are depicted as blue points in Fig. 7(b)). Based on this database, three GP models are generated for each objective accompanied by an expected hypervolume criterion to identify the next design (see Fig. 1 and its associated text). The selected design (given by specific values of the set of parameters) is then simulated with our DGTD fullwave solver. Then, new objective values are determined and used to enhance the three GP models. These steps are repeated till an adequately small EHI is reached.

The performed optimization iterations are represented by the black points in Fig. 7(b)) while the red points identify the set of non-dominated points in the objective space (Pareto front). The most striking result that emerges from these data is that 90 optimization iterations (black points) are enough to capture the Pareto front. The discussion about the convergence of the three metamodels is elaborated below (see Fig. 9 and its associated text). This striking peculiarity of the multiobjective EGO method makes it a viable alternative to the classical heuristic evolutionary algorithms where a considerable number of iterations are required to approximate the Pareto front.⁴⁶

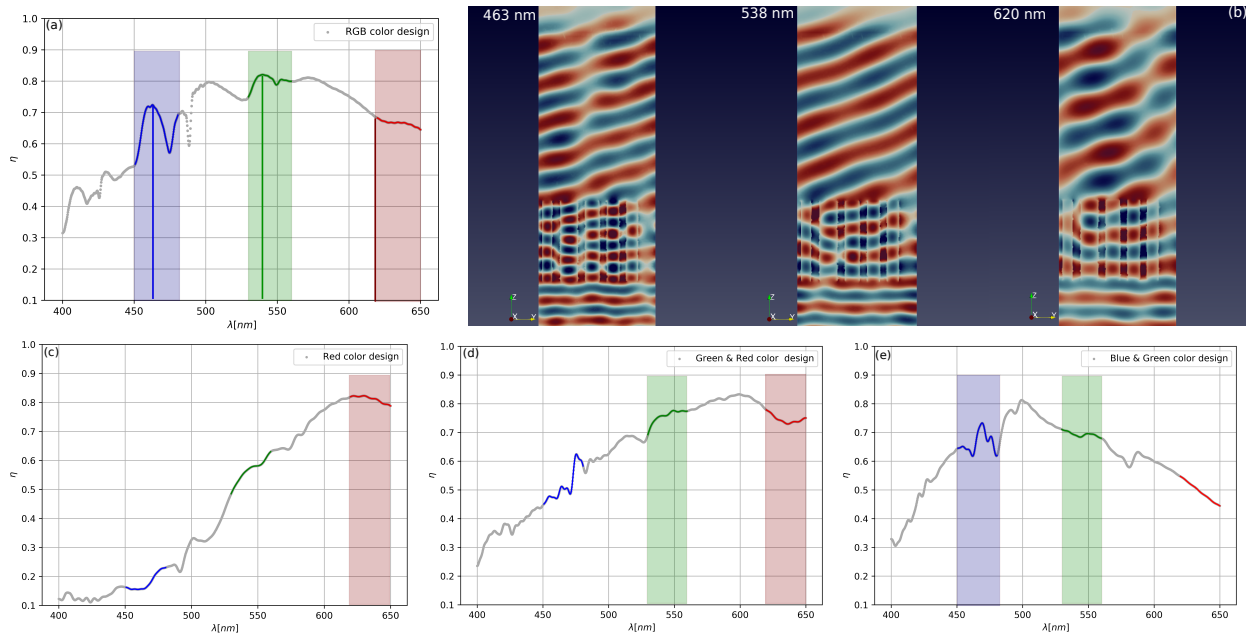


Figure 8: (a-b): results for the best middle point along the Pareto front shown in Fig. 7(b). (a): the deflection efficiency for the first order mode is represented by the gray curve as a function of the wavelength. The blue, green, and red parts on the gray curve denote the optimization interval defined for each color. The vertical color lines, refer to the wavelengths where the efficiencies attain their maximum in each interval. (b) $\Re(E_y)$ at the maximum efficiency in each interval. (c-e), optimization results for various designs along the Pareto front shown in Fig. 7(b). (c): refers to the optimized design for the red color, (d), for the green and red colors, and finally (e) for the blue and green colors. The corresponding optimization parameters are given in Tab. 2.

It is worth highlighting that the most beneficial attribute of any multiobjective optimization is the construction of the Pareto front, which materializes the trade-off between the

competing objectives. In Fig. 8, we present different optimized designs. Figs. 8(a-b) refers to a middle point along the Pareto front (point A in Fig. 7(b)) where all the objectives are optimized simultaneously; we refer to this design as the RGB design (the associated optimized parameters are given in the second column in Tab. 2). In Fig. 8(a), we plot the deflection efficiency of the first order mode for the RGB design. As it can be seen, the mean deflection efficiencies for the three regions are enhanced concurrently, and the average efficiency reaches 65.5%, 80.0%, and 66.5% for blue, green, and red colors, respectively. The vertical lines indicate the wavelengths where the maximum efficiency is achieved in each interval, namely 463 nm, 538 nm, and 620 nm, for blue, green, and red colors, respectively. The corresponding field profiles are plotted in Fig. 8(b) where the light bending is adequately presented for the three wavelengths with 72%, 82%, and 69% deflection efficiencies, respectively. For the red color region, one might decide to choose the efficiency at $\lambda = 600$ nm that corresponds to 75%, which is still in the red region. The most notable observation that emerges from the field profile comparison in Fig. 8(b) is the ability of the optimized nanoridges to treat the different longitudinal modes for the considered wavelengths. This peculiar treatment results in an average effective mode index profile for each wavelength to maximize the deflection efficiency for three wavelengths at the same time. Remarkably, this correlation is related to strong near field interactions between the elements, as it is depicted in Fig. 8(b). Crucially, these interactions are not identical across the three wavelengths and they depend on the number of longitudinal modes that propagate in each element for each wavelength. In other words, the optimization identifies the set of parameters that magnify the three objectives taking into account the strong near field coupling between the ridges. This appealing results cannot be achieved using the classical phase synthesizing approach where each ridge is placed based on its phase and transmission response for a given wavelength. Besides, these results further strengthened our confidence in our numerical methodology by combining a high-order fullwave solver with an efficient global optimization method.

In Figs. 8(c-e), we present different optimized designs along the Pareto front (points C-

Table 2: Optimization parameters for a four designs presented in Fig. 8(a) and Figs. 8(c-e), for the RGB, Red, Green-Red, and Blue-Green colors, respectively. The height of the nanoridges is fixed as $h = 1000$ nm, and the widths along x -direction are fixed as 100 nm. The distances between ridges are fixed as 90 nm. Besides, the period along x is given as 190 nm, while along y is 1500 nm.

Width (nm)	RGB	Red	Green-Red	Blue-Green
w_1	127.96	249.51	129.42	236.92
w_2	233.19	216.14	246.70	189.76
w_3	177.71	169.21	179.26	162.52
w_4	158.48	113.48	145.79	148.30
w_5	142.72	127.78	142.15	136.52

D in Fig. 7(b), respectively) to further extend the discussion and provide the reader with more insights about the usefulness of the multiobjective optimization. Figs. 8(c-e), refer to optimized designs where we focus on the red color, both the green and red colors, and finally both the blue and green colors, respectively. The corresponding optimization parameters are given in Tab. 2. These results emphasize the significant trade-off between the three objectives. We note that more than 80% of deflection efficiency can be achieved if one focuses only on a single objective as it is the case in Fig. 8(c), while the efficiency drops when two competing objectives are considered, as expected (see Figs. 8(d-e)). Nevertheless, thanks to our global multiobjective EGO method, an adequate balance between the three objectives is obtained as illustrated in Figs. 8(a-b). To the best of our knowledge, these results demonstrate the highest RGB light deflector efficiency based on realistic metasurface configuration.

Convergence of the RGB deflector design

In Fig. 9 (a-c), we study the leave-one-out predictions versus true values for each GP models, one for each objective, respectively. In these figures, each point corresponds to the prediction values from each metamodels as if the point was removed from the training set, compared to the exact value. In other words, for all the points along the line (for each sub figure), the predicted values deduced by the metamodels are equal to the true values. Obviously, we

are more interested in low values (minimization problem), where the fitting deduced by the three models are in a good agreement with the exact values. Besides (data not shown), the EHI for the last 30 iterations remains of the order of 10^{-2} which is another indication that 90 iterations are enough to approximate the Pareto front as given in Fig. 8(b).

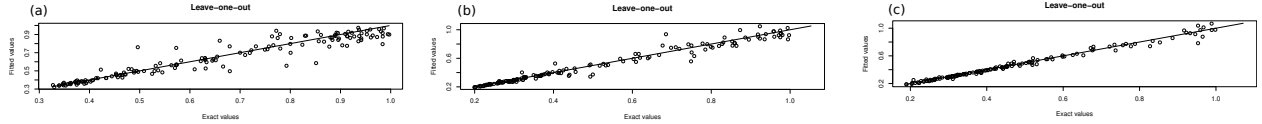


Figure 9: Illustration of the optimization convergence for RGB light deflector results presented in Fig. 7(b)

Additional information for the metalens

In this section, we provide additional data to complement our numerical results presented in the main manuscript. In Fig. 10(a) we provide additional information about the symmetry properties. Besides, in Fig. 10(a) we demonstrate the convergence of one of the optimized lenses. In Fig. 11 we discuss the optimization convergence of the first lens presented in Fig. 3. The associated parameters can be found in Tab. 3. Tab. 4 refers to the optimization parameters for the results presented in Fig. 5, while, the parameters for the design shown in Fig. 6 are shown in Tab. 5, where we focus only on the $\lambda = 640$ nm. Besides, we discuss further information for the fabrication procedure and the experimental characterization of the fabricated lenses.

Fabrication process

The metalenses were made of GaN pillars with $1 \mu\text{m}$ in height. They have been revealed by patterning a $1 \mu\text{m}$ thick GaN layer grown on a c-plan sapphire substrate using a Molecular Beam Epitaxy. Conventional electron beam lithography (EBL) was used to expose a double layer of ≈ 200 nm PMMA resist (495A4) spin-coated on the GaN thin-film and then baked on a hot plate at 125°C . E-beam resist exposure was then performed at 20 keV (using a

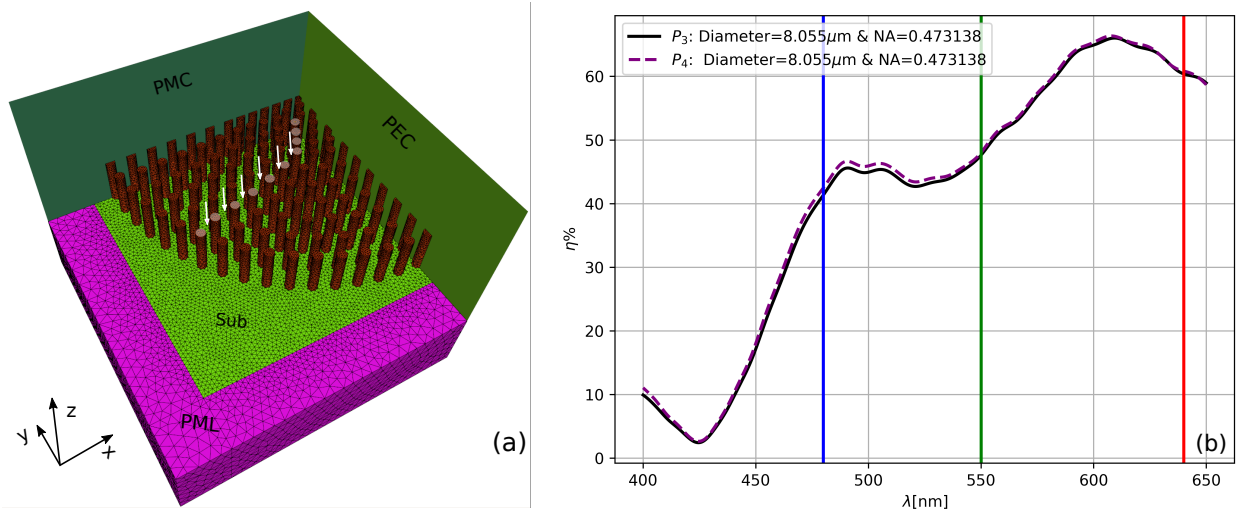


Figure 10: (a): 3D Schematic view for one quarter of 3D metalens under investigation (see Fig. 2 for the $x - y$ view). The red cylinders are made of GaN and the substrate is composed of Al_2O_3 . The optimized cylinders are highlighted in white circles along with the distance between the outer rings (white arrows). We consider a normally incident plane wave from the substrate with electric field polarized along x -axis. Therefore, in order to mimic the full geometry, we consider a perfect electric conducting (PEC) condition on the right most faces (where the electric field is oscillating) and perfect magnetic conducting (PMC) along the front face. During the optimization iterations, we consider a mesh of size corresponding to 5 points per wavelength inside the cylinders. In general, the number of cells is almost 800,000. In the framework of our DGTD fullwave solver, we consider a third order polynomial P_3 interpolation to approximate the electromagnetic fields, which is enough to get accurate solutions during all the optimization iterations. The justification is shown in (b) where the agreement between the results obtained for P_3 and P_4 interpolations (for the results presented in Fig. 3) is fully demonstrated. Each iteration takes almost 1 h using 720 cores. The numerical experiments presented in this paper were carried out using the PlaFRIM experimental testbed, supported by Inria, CNRS (LABRI and IMB), Université de Bordeaux, Bordeaux INP and Conseil Régional d'Aquitaine.

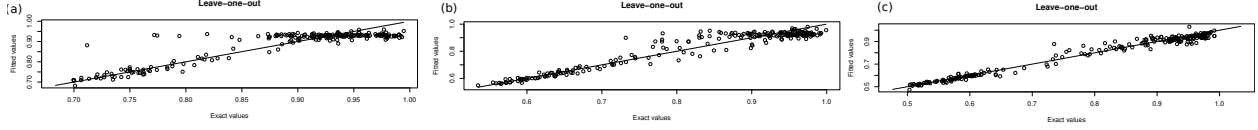


Figure 11: Illustration of the optimization convergence for the results presented in Fig. 3. Here we study the leave-one-out predictions versus true values for each GP models. (a) for first objective, (b) for the second objective, and (c) for the third objective. In these figures, each point corresponds to the prediction, if the point was removed from the training set, compared to the exact value. In other words, for all the points along the line, the predicted values deduced by the metamodels are equal to the true values. A subtlety is that all values are still used to estimate the parameters of the GP models and not removed. Hence they do influence the results in an indirect way. Plateaus around one at the top (especially for the first two objectives) could indicate that a large part of the design space has this value (see blue points in Fig. 3(a)). However, flat regions are hard to model for GPs, hence worsening prediction. Fortunately here we are more interested in low values (maximize the the efficiency in this minimization problem), that are better fitted for the three models.

Table 3: Optimization parameters for the metalens presented in Fig. 3 with diameter $D = 8.055 \mu\text{m}$ and $\text{NA} = 0.473138$. The first two columns refer to the number of rings (first) and the associated number of cylinders (second). The third column gives the diameter of the cylinders in each ring. The fourth column indicates the distances between rings (for instance, $\text{Ring}_{2,1}$ refers to the distance between the second and the first rings). Their values are given in the last column.

Ring	cylinders	Radius (nm)	Distance indicators	Distance values in nm
Central	1	110.000	-	-
1	7	100.000	$\text{Ring}_{1,cent}$	100.000
2	13	100.000	$\text{Ring}_{2,1}$	100.000
3	15	100.000	$\text{Ring}_{3,2}$	100.000
4	21	94.6262	$\text{Ring}_{4,3}$	100.000
5	27	91.3074	$\text{Ring}_{5,4}$	100.000
6	33	85.7489	$\text{Ring}_{6,5}$	100.000
7	37	79.9027	$\text{Ring}_{7,6}$	188.312
8	41	70.8879	$\text{Ring}_{8,7}$	191.255
9	45	62.1650	$\text{Ring}_{9,8}$	216.618
10	49	45.0000	$\text{Ring}_{10,9}$	250.000
11	53	100.000	$\text{Ring}_{11,10}$	120.437
12	65	69.5238	$\text{Ring}_{12,11}$	192.588

Table 4: Optimization parameters for the extended metalens presented in Fig. 5 with diameter $D = 10.22 \mu\text{m}$ and $\text{NA} = 0.56$. The first 11 rows are identical to the the ones in Tab. 3 (the meaning of the columns remains the same). The green color refers to the optimized rings in the extended design.

Ring	cylinders	Radius (nm)	Distance indicators	Distance values in nm
Central	1	110.000	-	-
1	7	100.000	Ring _{1,cent}	100.000
2	13	100.000	Ring _{2,1}	100.000
3	15	100.000	Ring _{3,2}	100.000
4	21	94.6262	Ring _{4,3}	100.000
5	27	91.3074	Ring _{5,4}	100.000
6	33	85.7489	Ring _{6,5}	100.000
7	37	79.9027	Ring _{7,6}	188.312
8	41	70.8879	Ring _{8,7}	191.255
9	45	62.1650	Ring _{9,8}	216.618
10	49	45.0000	Ring _{10,9}	250.000
11	53	100.000	Ring _{11,10}	120.437
12	65	68.0160	Ring _{12,11}	192.588
13	105	51.5016	Ring _{13,12}	250.000
14	105	90.5210	Ring _{14,13}	228.898
15	105	61.0380	Ring _{15,14}	111.765

Table 5: Optimization parameters for the lens given in Fig. 6 with diameter $D = 10.66 \mu\text{m}$ and $\text{NA} = 0.5755$. The first 11 rows are identical to the the ones in Tab. 3 (the meaning of the columns remains the same). The green color refers to the optimized rings in the extended design.

Ring	cylinders	Radius (nm)	Distance indicators	Distance values in nm
Central	1	110.000	-	-
1	7	100.000	Ring _{1,cent}	100.000
2	13	100.000	Ring _{2,1}	100.000
3	15	100.000	Ring _{3,2}	100.000
4	21	94.6262	Ring _{4,3}	100.000
5	27	91.3074	Ring _{5,4}	100.000
6	33	85.7489	Ring _{6,5}	100.000
7	37	79.9027	Ring _{7,6}	188.312
8	41	70.8879	Ring _{8,7}	191.255
9	45	62.1650	Ring _{9,8}	216.618
10	49	45.0000	Ring _{10,9}	250.000
11	53	100.000	Ring _{11,10}	120.437
12	65	87.209	Ring _{12,11}	192.588
13	105	45.000	Ring _{13,12}	250.000
14	105	100.000	Ring _{14,13}	250.000
15	105	88.443	Ring _{15,14}	202.365

Raith ElphyPlus, Zeiss Supra 40), followed by PMMA development using a 3:1 IPA:MIBK solution. After development, a 50 nm layer of Ni was deposited using e-beam evaporation to perform a metallic film liftoff by immersing the sample into acetone solution for 2 h. The resulting Ni pattern was utilized as a hard mask during the reactive ion etching (RIE, Oxford system with a plasma composed of Cl₂, CH₄, Ar gases, with flows of 13, 2, and 2 sccm, respectively) to transfer the pattern in the GaN layer. Finally, the Ni hard mask on the top of GaN nanopillars was removed using chemical etching with a 1:2 HCl/HNO₃ solution.

Characterization setup

To characterize the fabricated metalenses, we used a home-made inverted optical microscope as depicted in fig. 12. The illumination part consists of LEDs centred at three different wavelengths (490, 550 and 660 nm). The LEDs are positioned in Köhler optical scheme in order to illuminate the sample with controlled spot size (diaphragm D1) and numerical aperture (Diaphragm D2). The light passing through the metalens sample is collected by a microscope objective positioned on moving stage to detect different planes along the optical axis Oz (perform z-scan). It is worth-noting that in this configuration the focal plane of the metalens is conjugated with the plane of the diaphragm D2. The light is then sent to the tube lens and finally to the wavefront analyzer. The latter is capable of measuring both intensity and phase maps of incoming light (see ref [S.Khadir et al. ACS Photonics 2021] for more information)

Cross section of the focusing spots

References

- (1) Astilean, S.; Lalanne, P.; Chavel, P.; Cambril, E.; Launois, H. High-efficiency subwavelength diffractive element patterned in a high-refractive-index material for 633 nm.

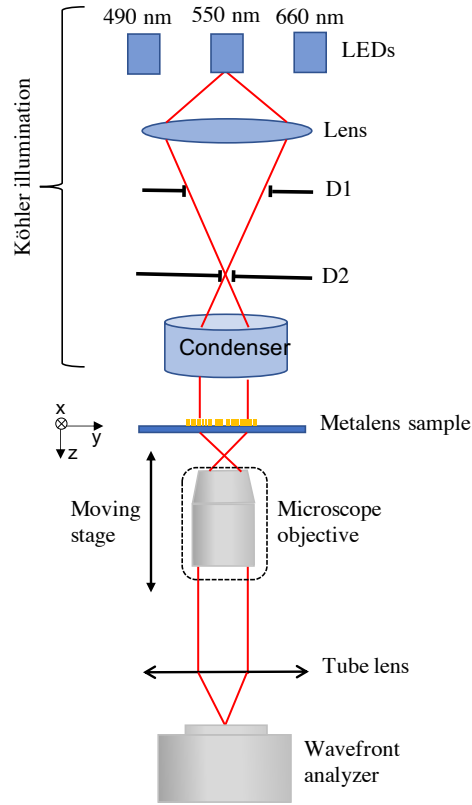


Figure 12: Scheme of the optical setup used to characterize the metalenses. LEDs with different wavelengths combined to a Köhler configuration illuminates the sample with a light beam controlled in wavelength, size, and numerical aperture. The light passing through the metalens sample is collected by a microscope objective lens and sent to the QLSI wavefront analyzer. The microscope objective is mounted on moving stage to perform z-scan of the light passing through the metalens

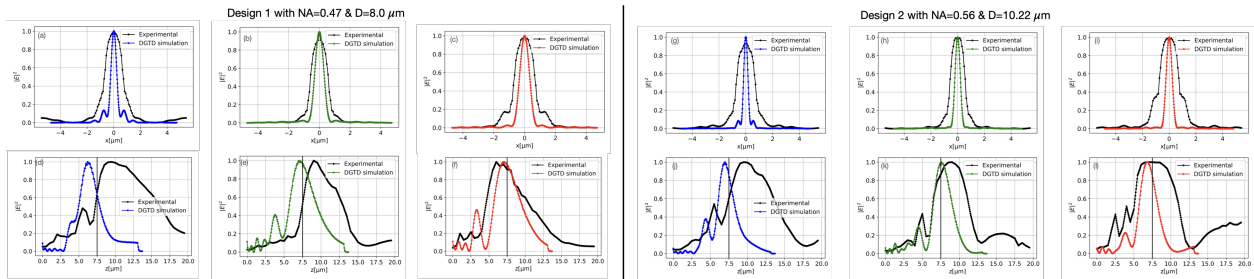


Figure 13: Intensity profile cuts for the first design depicted in Fig. 3 (first column) and the second design illustrated in Fig. 5 (second column). The first row for the 1D cut along x axis at the focal distance $F = 7.5 \mu\text{m}$, while the second one for the cut along z axis at the center of the lens. See the main text for more details.

- Optics letters* **1998**, *23*, 552–554.
- (2) Lalanne, P.; Astilean, S.; Chavel, P.; Cambril, E.; Launois, H. Design and fabrication of blazed binary diffractive elements with sampling periods smaller than the structural cutoff. *JOSA A* **1999**, *16*, 1143–1156.
- (3) Yu, N.; Genevet, P.; Kats, M. A.; Aieta, F.; Tetienne, J.-P.; Capasso, F.; Gaburro, Z. Light Propagation with Phase Discontinuities: Generalized Laws of Reflection and Refraction. *Science* **2011**, *334*, 333–337.
- (4) Sun, S.; He, Q.; Xiao, S.; Xu, Q.; Li, X.; Zhou, L. Gradient-index meta-surfaces as a bridge linking propagating waves and surface waves. *Nature materials* **2012**, *11*, 426.
- (5) Lin, D.; Fan, P.; Hasman, E.; Brongersma, M. L. Dielectric gradient metasurface optical elements. *Science* **2014**, *345*, 298–302.
- (6) Lee, M.-S. L.; Lalanne, P.; Rodier, J.; Chavel, P.; Cambril, E.; Chen, Y. Imaging with blazed-binary diffractive elements. *Journal of Optics A: Pure and Applied Optics* **2002**, *4*, S119.
- (7) Zhu, A. Y.; Kuznetsov, A. I.; Luk'yanchuk, B.; Engheta, N.; Genevet, P. Traditional and emerging materials for optical metasurfaces. *Nanophotonics* **2017**, *6*, 452–471.
- (8) Genevet, P.; Capasso, F.; Aieta, F.; Khorasaninejad, M.; Devlin, R. Recent advances in planar optics: from plasmonic to dielectric metasurfaces. *Optica* **2017**, *4*, 139–152.
- (9) Chen, H.-T.; Taylor, A. J.; Yu, N. A review of metasurfaces: physics and applications. *Reports on progress in physics* **2016**, *79*, 076401.
- (10) Salandrino, A.; Engheta, N. Far-field subdiffraction optical microscopy using metamaterial crystals: Theory and simulations. *Phys. Rev. B* **2006**, *74*, 075103.
- (11) Krasnok, A.; Tymchenko, M.; Alù, A. Nonlinear metasurfaces: a paradigm shift in nonlinear optics. *Materials Today* **2018**, *21*, 8 – 21.

- (12) Bekenstein, R.; Pikovski, I.; Pichler, H.; Shahmoon, E.; Yelin, S.; Lukin, M. Quantum metasurfaces with atom arrays. *Nature Physics* **2020**, *16*, 676–681.
- (13) Molesky, S.; Lin, Z.; Piggott, A. Y.; Jin, W.; Vuckovic, J.; Rodriguez, A. W. Outlook for inverse design in nanophotonics. *arXiv preprint arXiv:1801.06715* **2018**,
- (14) Yao, K.; Unni, R.; Zheng, Y. Intelligent nanophotonics: merging photonics and artificial intelligence at the nanoscale. *Nanophotonics* **2019**, *8*, 339–366.
- (15) Elsayy, M. M. R.; Lanteri, S.; Duvigneau, R.; Brière, G.; Mohamed, M. S.; Genevet, P. Global optimization of metasurface designs using statistical learning methods. *Scientific Reports* **2019**, *9*.
- (16) Elsayy, M. M. R.; Lanteri, S.; Duvigneau, R.; Fan, J. A.; Genevet, P. Numerical Optimization Methods for Metasurfaces. *Laser & Photonics Reviews* **2020**, *14*, 1900445.
- (17) Marler, R. T.; Arora, J. S. The weighted sum method for multi-objective optimization: new insights. *Structural and multidisciplinary optimization* **2010**, *41*, 853–862.
- (18) Kim, I. Y.; De Weck, O. Adaptive weighted sum method for multiobjective optimization: a new method for Pareto front generation. *Structural and multidisciplinary optimization* **2006**, *31*, 105–116.
- (19) Naidu, K.; Mokhlis, H.; Bakar, A. A. Multiobjective optimization using weighted sum artificial bee colony algorithm for load frequency control. *International Journal of Electrical Power & Energy Systems* **2014**, *55*, 657–667.
- (20) Jafar-Zanjani, S.; Inampudi, S.; Mosallaei, H. Adaptive genetic algorithm for optical metasurfaces design. *Scientific reports* **2018**, *8*, 1–16.
- (21) Tang, D.; Chen, L.; Liu, J. Visible achromatic super-oscillatory metasurfaces for sub-diffraction focusing. *Optics express* **2019**, *27*, 12308–12316.

- (22) Lalbakhsh, A.; Afzal, M. U.; Esselle, K. P. Multiobjective particle swarm optimization to design a time-delay equalizer metasurface for an electromagnetic band-gap resonator antenna. *IEEE Antennas and Wireless Propagation Letters* **2016**, *16*, 912–915.
- (23) Allen, K. W.; Dykes, D. J.; Reid, D. R.; Lee, R. T. Multi-Objective Genetic Algorithm Optimization of Frequency Selective Metasurfaces to Engineer Ku-Passband Filter Responses. *Progress In Electromagnetics Research* **2020**, *167*, 19–30.
- (24) Marler, R. T.; Arora, J. S. Survey of multi-objective optimization methods for engineering. *Structural and multidisciplinary optimization* **2004**, *26*, 369–395.
- (25) Deb, K. *Multi-objective optimization using evolutionary algorithms*; John Wiley & Sons, 2001; Vol. 16.
- (26) Coello, C. A. C.; Lamont, G. B.; Van Veldhuizen, D. A., et al. *Evolutionary algorithms for solving multi-objective problems*; Springer, 2007; Vol. 5.
- (27) Zhou, A.; Qu, B.-Y.; Li, H.; Zhao, S.-Z.; Suganthan, P. N.; Zhang, Q. Multiobjective evolutionary algorithms: A survey of the state of the art. *Swarm and Evolutionary Computation* **2011**, *1*, 32–49.
- (28) Li, H.; Zhang, Q. Multiobjective optimization problems with complicated Pareto sets, MOEA/D and NSGA-II. *IEEE transactions on evolutionary computation* **2008**, *13*, 284–302.
- (29) Hadka, D.; Reed, P. Borg: An auto-adaptive many-objective evolutionary computing framework. *Evolutionary computation* **2013**, *21*, 231–259.
- (30) Dhiman, G.; Singh, K. K.; Slowik, A.; Chang, V.; Yildiz, A. R.; Kaur, A.; Garg, M. EMoSOA: a new evolutionary multi-objective seagull optimization algorithm for global optimization. *International Journal of Machine Learning and Cybernetics* **2020**, 1–26.

- (31) Murata, T.; Ishibuchi, H. MOGA: multi-objective genetic algorithms. IEEE international conference on evolutionary computation. 1995; pp 289–294.
- (32) Konak, A.; Coit, D. W.; Smith, A. E. Multi-objective optimization using genetic algorithms: A tutorial. *Reliability Engineering & System Safety* **2006**, *91*, 992–1007.
- (33) Deb, K.; Pratap, A.; Agarwal, S.; Meyarivan, T. A fast and elitist multiobjective genetic algorithm: NSGA-II. *IEEE transactions on evolutionary computation* **2002**, *6*, 182–197.
- (34) Igel, C.; Hansen, N.; Roth, S. Covariance matrix adaptation for multi-objective optimization. *Evolutionary computation* **2007**, *15*, 1–28.
- (35) Coello, C. C.; Lechuga, M. S. MOPSO: A proposal for multiple objective particle swarm optimization. Proceedings of the 2002 Congress on Evolutionary Computation. CEC’02 (Cat. No. 02TH8600). 2002; pp 1051–1056.
- (36) Mostaghim, S.; Teich, J. Strategies for finding good local guides in multi-objective particle swarm optimization (MOPSO). Proceedings of the 2003 IEEE Swarm Intelligence Symposium. SIS’03 (Cat. No. 03EX706). 2003; pp 26–33.
- (37) Coello, C. A. C.; Pulido, G. T.; Lechuga, M. S. Handling multiple objectives with particle swarm optimization. *IEEE Transactions on evolutionary computation* **2004**, *8*, 256–279.
- (38) Reyes-Sierra, M.; Coello, C. C., et al. Multi-objective particle swarm optimizers: A survey of the state-of-the-art. *International journal of computational intelligence research* **2006**, *2*, 287–308.
- (39) Gagnon, D.; Dumont, J.; Dubé, L. J. Multiobjective optimization in integrated photonics design. *Optics Letters* **2013**, *38*, 2181–2184.

- (40) Nagar, J.; Werner, D. H. A comparison of three uniquely different state of the art and two classical multiobjective optimization algorithms as applied to electromagnetics. *IEEE Transactions on Antennas and Propagation* **2017**, *65*, 1267–1280.
- (41) Nagar, J.; Werner, D. H. Multiobjective Optimization for Electromagnetics and Optics: An Introduction and Tutorial Based on Real-World Applications. *IEEE Antennas and Propagation Magazine* **2018**, *60*, 58–71.
- (42) Liu, Z.; Liu, X.; Xiao, Z.; Lu, C.; Wang, H.-Q.; Wu, Y.; Hu, X.; Liu, Y.-C.; Zhang, H.; Zhang, X. Integrated nanophotonic wavelength router based on an intelligent algorithm. *Optica* **2019**, *6*, 1367–1373.
- (43) Allen, K. W.; Dykes, D. J.; Reid, D. R.; Bean, J. A.; Landgren, D. W.; Lee, R. T.; Denison, D. R. Metasurface engineering via evolutionary processes. 2017 IEEE National Aerospace and Electronics Conference (NAECON). 2017; pp 172–178.
- (44) Wiecha, P. R.; Arbouet, A.; Girard, C.; Lecestre, A.; Larrieu, G.; Paillard, V. Evolutionary multi-objective optimization of colour pixels based on dielectric nanoantennas. *Nature nanotechnology* **2017**, *12*, 163.
- (45) Wiecha, P. R.; Arbouet, A.; Girard, C.; Lecestre, A.; Larrieu, G.; Paillard, V. Multi-resonant silicon nanoantennas by evolutionary multi-objective optimization. *Computational Optics II*. 2018; p 1069402.
- (46) Whiting, E. B.; Campbell, S. D.; Kang, L.; Werner, D. H. Meta-atom library generation via an efficient multi-objective shape optimization method. *Opt. Express* **2020**, *28*, 24229–24242.
- (47) Campbell, S. D.; Zhu, D. Z.; Whiting, E. B.; Nagar, J.; Werner, D. H.; Werner, P. L. Advanced multi-objective and surrogate-assisted optimization of topologically diverse metasurface architectures. *Metamaterials, Metadevices, and Metasystems 2018*. 2018; p 107190U.

- (48) So, S.; Badloe, T.; Noh, J.; Rho, J.; Bravo-Abad, J. Deep learning enabled inverse design in nanophotonics. *Nanophotonics* **2020**,
- (49) Yao, K.; Unni, R.; Zheng, Y. Intelligent nanophotonics: merging photonics and artificial intelligence at the nanoscale. *Nanophotonics* **2019**, *8*, 339–366.
- (50) Wiecha, P. R.; Muskens, O. L. Deep learning meets nanophotonics: A generalized accurate predictor for near fields and far fields of arbitrary 3D nanostructures. *Nano Letters* **2019**,
- (51) Kiarashinejad, Y.; Zandehshahvar, M.; Abdollahramezani, S.; Hemmatyar, O.; Pourabolghasem, R.; Adibi, A. Knowledge Discovery in Nanophotonics Using Geometric Deep Learning. *Advanced Intelligent Systems* **2020**, *2*, 1900132.
- (52) Kudyshev, Z. A.; Kildishev, A. V.; Shalaev, V. M.; Boltasseva, A. Machine-Learning-Assisted Metasurface Design for High-Efficiency Thermal Emitter Optimization. *arXiv preprint arXiv:1910.12741* **2019**,
- (53) Kiarashinejad, Y.; Abdollahramezani, S.; Adibi, A. Deep learning approach based on dimensionality reduction for designing electromagnetic nanostructures. *npj Computational Materials* **2020**, *6*, 1–12.
- (54) Campbell, S. D.; Sell, D.; Jenkins, R. P.; Whiting, E. B.; Fan, J. A.; Werner, D. H. Review of numerical optimization techniques for meta-device design. *Optical Materials Express* **2019**, *9*, 1842–1863.
- (55) Inampudi, S.; Mosallaei, H. Neural network based design of metagratings. *Applied Physics Letters* **2018**, *112*, 241102.
- (56) Liu, Z.; Zhu, D.; Rodrigues, S.; Lee, K.-T.; Cai, W. A Generative Model for the Inverse Design of Metasurfaces. *Nano letters* **2018**,

- (57) Jiang, J.; Fan, J. A. Global optimization of dielectric metasurfaces using a physics-driven neural network. *Nano letters* **2019**, *19*, 5366–5372.
- (58) Jiang, J.; Fan, J. A. Simulator-based training of generative neural networks for the inverse design of metasurfaces. *Nanophotonics* **2019**, *1*.
- (59) Jiang, J.; Fan, J. A. Multiobjective and categorical global optimization of photonic structures based on ResNet generative neural networks. *Nanophotonics* **2020**, *1*.
- (60) An, S.; Zheng, B.; Tang, H.; Shalaginov, M. Y.; Zhou, L.; Li, H.; Gu, T.; Hu, J.; Fowler, C.; Zhang, H. Generative multi-functional meta-atom and metasurface design networks. *arXiv preprint arXiv:1908.04851* **2019**,
- (61) Naseri, P.; Hum, S. V. A Generative Machine Learning-Based Approach for Inverse Design of Multilayer Metasurfaces. *arXiv preprint arXiv:2008.02074* **2020**,
- (62) Elsayy, M. M. R.; Lanteri, S.; Duvigneau, R.; Brière, G.; Mohamed, M. S.; Genevet, P. Global optimization of metasurface designs using statistical learning methods. *Scientific Reports* **2019**, *9*.
- (63) Jones, D. Efficient global optimization of expensive black-box functions. *Journal of Global Optimization* **1998**, *13*.
- (64) Jones, D. A taxonomy of global optimization methods based on response surfaces. *Journal of Global Optimization* **2001**, *21*, 345–383.
- (65) Forestiere, C.; He, Y.; Wang, R.; Kirby, R. M.; Dal Negro, L. Inverse design of metal nanoparticles' morphology. *ACS Photonics* **2015**, *3*, 68–78.
- (66) Gramacy, R. B. *Surrogates: Gaussian Process Modeling, Design, and Optimization for the Applied Sciences*; CRC Press, 2020.

- (67) Shahriari, B.; Swersky, K.; Wang, Z.; Adams, R. P.; de Freitas, N. Taking the human out of the loop: A review of Bayesian optimization. *Proceedings of the IEEE* **2016**, *104*, 148–175.
- (68) Emmerich, M. Single-and multi-objective evolutionary design optimization assisted by gaussian random field metamodels. *Dissertation, LS11, FB Informatik, Universität Dortmund, Germany* **2005**,
- (69) Palar, P. S.; Zuhail, L. R.; Chugh, T.; Rahat, A. On the impact of covariance functions in multi-objective Bayesian optimization for engineering design. AIAA Scitech 2020 Forum. 2020; p 1867.
- (70) Emmerich, M. T.; Deutz, A. H.; Klinkenberg, J. W. Hypervolume-based expected improvement: Monotonicity properties and exact computation. *Evolutionary Computation (CEC), 2011 IEEE Congress on*. 2011; pp 2147–2154.
- (71) Emmerich, M. T.; Giannakoglou, K. C.; Naujoks, B. Single-and multiobjective evolutionary optimization assisted by Gaussian random field metamodels. *IEEE Transactions on Evolutionary Computation* **2006**, *10*, 421–439.
- (72) Binois, M.; Picheny, V. GPareto: An R Package for Gaussian-Process-Based Multi-Objective Optimization and Analysis. *Journal of Statistical Software* **2019**, *89*, 1–30.
- (73) Binois, M.; Picheny, V. GPareto: Gaussian Processes for Pareto Front Estimation and Optimization. 2020; R package version 1.1.4.1.
- (74) Lanteri, S.; Scheid, C.; Viquerat, J. Analysis of a generalized dispersive model coupled to a DGTD method with application to nanophotonics. *SIAM J. Sci. Comp.* **2017**, *39*, 831–859.
- (75) Viquerat, J. Simulation of electromagnetic waves propagation in nano-optics with a

- high-order discontinuous Galerkin time-domain method. Ph.D. thesis, University of Nice-Sophia Antipolis, 2015.
- (76) Diogenes: A Discontinuous-Galerkin based software suite for nano-optics. <https://diogenes.inria.fr/>.
- (77) Elsayy, M. M. R.; Hassan, K.; Boutami, S.; Lanteri, S. Bayesian optimization and rigorous modelling of a highly efficient 3D metamaterial mode converter. *OSA Continuum* **2020**, *3*, 1721–1729.
- (78) Byrnes, S. J.; Lenef, A.; Aieta, F.; Capasso, F. Designing large, high-efficiency, high-numerical-aperture, transmissive meta-lenses for visible light. *Optics express* **2016**, *24*, 5110–5124.
- (79) Wang, S.; Wu, P. C.; Su, V.-C.; Lai, Y.-C.; Chu, C. H.; Chen, J.-W.; Lu, S.-H.; Chen, J.; Xu, B.; Kuan, C.-H., et al. Broadband achromatic optical metasurface devices. *Nature communications* **2017**, *8*, 1–9.
- (80) Wang, S.; Wu, P. C.; Su, V.-C.; Lai, Y.-C.; Chen, M.-K.; Kuo, H. Y.; Chen, B. H.; Chen, Y. H.; Huang, T.-T.; Wang, J.-H., et al. A broadband achromatic metalens in the visible. *Nature nanotechnology* **2018**, *13*, 227.
- (81) Ndao, A.; Hsu, L.; Ha, J.; Park, J.-H.; Chang-Hasnain, C.; Kanté, B. Octave bandwidth photonic fishnet-achromatic-metalens. *Nature communications* **2020**, *11*, 1–6.
- (82) Balli, F.; Sultan, M.; Lami, S. K.; Hastings, J. T. A hybrid achromatic metalens. *Nature communications* **2020**, *11*, 1–8.
- (83) Chung, H.; Miller, O. D. High-NA achromatic metalenses by inverse design. *Optics Express* **2020**, *28*, 6945–6965.
- (84) Lin, Z.; Johnson, S. G. Overlapping domains for topology optimization of large-area metasurfaces. *Optics express* **2019**, *27*, 32445–32453.

- (85) Lin, Z.; Liu, V.; Pestourie, R.; Johnson, S. G. Topology optimization of freeform large-area metasurfaces. *Opt. Express* **2019**, *27*, 15765–15775.
- (86) Zhan, A.; Fryett, T. K.; Colburn, S.; Majumdar, A. Inverse design of optical elements based on arrays of dielectric spheres. *Applied optics* **2018**, *57*, 1437–1446.
- (87) Backer, A. S. Computational inverse design for cascaded systems of metasurface optics. *Optics express* **2019**, *27*, 30308–30331.
- (88) Mansouree, M.; McClung, A.; Samudrala, S.; Arbabi, A. Large-Scale Parametrized Metasurface Design Using Adjoint Optimization. *ACS Photonics* **2021**, *8*, 455–463.
- (89) Zhang, D.; Qin, F.; Zhang, Q.; Liu, Z.; Wei, G.; Xiao, J. J. Segmented Bayesian optimization of meta-gratings for sub-wavelength light focusing. *JOSA B* **2020**, *37*, 181–187.
- (90) Pestourie, R.; Pérez-Arancibia, C.; Lin, Z.; Shin, W.; Capasso, F.; Johnson, S. G. Inverse design of large-area metasurfaces. *Optics express* **2018**, *26*, 33732–33747.
- (91) Christiansen, R. E.; Sigmund, O. A tutorial for inverse design in photonics by topology optimization. *arXiv preprint arXiv:2008.11816* **2020**,
- (92) Yağcı, H. B.; Demir, H. V. “Meta-atomless” architecture based on an irregular continuous fabric of coupling-tuned identical nanopillars enables highly efficient and achromatic metasurfaces. *Applied Physics Letters* **2021**, *118*, 081105.
- (93) Liang, H.; Martins, A.; Borges, B.-H. V.; Zhou, J.; Martins, E. R.; Li, J.; Krauss, T. F. High performance metalenses: numerical aperture, aberrations, chromaticity, and trade-offs. *Optica* **2019**, *6*, 1461–1470.
- (94) Presutti, F.; Monticone, F. Focusing on bandwidth: achromatic metalens limits. *Optica* **2020**, *7*, 624–631.

- (95) Chen, W. T.; Zhu, A. Y.; Sisler, J.; Bharwani, Z.; Capasso, F. A broadband achromatic polarization-insensitive metalens consisting of anisotropic nanostructures. *Nature communications* **2019**, *10*, 1–7.
- (96) Khadir, S.; Andr en, D.; Verre, R.; Song, Q.; Monneret, S.; Genevet, P.; K all, M.; Baffou, G. Metasurface optical characterization using quadriwave lateral shearing interferometry. *ACS photonics* **2021**, *8*, 603–613.